

# Supplementary Materials for

## Tracking Changes in Magma Transport from Very-Long-Period seismic signals at Piton de la Fournaise volcano

Zacharie Duputel<sup>1,2\*</sup>, Valérie Ferrazzini<sup>1,2</sup>, Cyril Journeau<sup>3,4</sup>, Philippe Catherine<sup>1,2</sup>, Philippe Kowalski<sup>1,2</sup> and Aline Peltier<sup>1,2</sup>

<sup>1</sup>Observatoire Volcanologique du Piton de la Fournaise, Institut de Physique du Globe de Paris, La Plaine des Cafres, France.

<sup>2</sup>Université Paris Cité, Institut de Physique du Globe de Paris, CNRS, Paris, France.

<sup>3</sup>Institut des Sciences de la Terre, Université Grenoble Alpes, CNRS (UMR 5275), Grenoble, France.

<sup>4</sup>Department of Earth Sciences, University of Oregon, Eugene, OR, USA.

\*Corresponding author. Email: [duputel@ipgp.fr](mailto:duputel@ipgp.fr)

### This PDF file includes:

Text S1-S8  
Movie captions S1 to S2  
Figs. S1 to S30

### Other Supplementary Materials for this manuscript include the following:

Movies S1 to S2

### Text S1. Volcano-tectonic earthquake detection and relocation

To analyze the volcano-tectonic (VT) swarm preceding the August-October 2015 eruption, we used template matching detections produced automatically at the Piton de la Fournaise Observatory (Duputel et al., 2019; Lengliné et al., 2016). This quasi real-time approach relies on a template catalog including the last 1,000 events manually located in the shallow part of the volcano edifice. The detection was performed using vertical components of stations BOR, BON and SNE after band-pass filtering in the 5-25 Hz passband. The detected earthquakes were then re-located using a double-difference relative location algorithm using P and S wave differential travel times measured by cross-correlation (Waldhauser and Ellsworth, 2000). This resulted in a final set of 361 relocated VT events during the pre-eruptive swarm of the August-October 2015 eruption (see Fig. 1A).

## **Text S2. GNSS displacements**

In 2015, the GNSS (Global Navigation Satellite System) network was composed of 24 permanent stations recording at a sampling rate of one measurement each 30 sec, and transmitting their data once a day to the OVPF. Daily post-processing solution was calculated with the GAMIT/GLOBK software package (Herring, T. A. et al., 2010) with a mm-precision on the horizontal components and 1-2 cm on the vertical one. Calculations take into consideration the precise ephemerides of the international GNSS Service (IGS); a stable support network of 20 IGS stations in and around the Indian Ocean area; a tested parameterization of the troposphere; and models of ocean loading, Earth and lunar tides. Data were corrected from plate motion. On Fig. 3, we show relative baseline changes (i.e., distance changes) for one GNSS station pair (SNE-DSR) at the summit of the volcano, where increasing distances indicate volcano inflation, while decreasing distances reflect edifice deflation. To estimate the associated measurement uncertainty, we computed the standard deviation of the time-series relative to a polynomial fit during inter-eruptive periods between June 2015 and May 2016 (see Fig. S1). The resulting noise level is ~2mm.

GNSS data during the rapid summit deflation prior to the first rest period was inverted for using the point compound dislocation model (Beauducel et al., 2020b, 2020a; Nikkhoo et al., 2017). We used daily time-series processed using the GIPSY-OASIS software in Precise Point Positioning (PPP) mode (Zumberge et al., 1997). The resulting model shown in Fig. S22 indicates the contraction of a vertical ellipsoid above the shallow reservoir. Given the location and geometry of the dislocation, we interpret it as the contraction of the dike feeding the eruption during the second VLP swarm. The ellipsoid geometry is consistent with the orientation of oscillating tensile cracks derived from moment tensor inversions of VLP signals (cf., Fig. 7).

A network of stainless steel benchmarks (75 in 2015) has also been established on the terminal cone to increase density of field measurements. The position of the benchmarks are re-measured after each magma injection during field campaigns. The receivers used during the 2015 surveys were the multi-frequency, multi-constellation ProMark 800 GNSS Surveying System from Ashtech. The acquisition time at each point was 3 min with a rate of 1 measurement per second, allowing a data precision of about 2.5 cm on the horizontal component and 4 cm on the vertical one. These data were post-processed with the Spectra Precision Survey Office software and referenced to the permanent GITG station located just outside of the north-western part of the Enclos Fouqué caldera (~4 km from the summit). To characterize the deformation associated to the August 24, 2015 dike injection shown in Fig. 2, we considered data acquired before the dike injection on August 10 and 11 and after the dike injection on August 28 and September 1.

## **Text S3. Orientation of broadband seismometers**

To check the horizontal orientation of broadband sensors, we compared observed seismograms with synthetic waveforms computed for teleseismic earthquakes at long period (in the 100-150 s passband). To maximize the long-period signal to noise ratio, we focused on very large teleseismic earthquakes: the 2015 Mw=7.3 Gorkha earthquake and the 2015 Mw=8.3 Illapel earthquake. Synthetics were computed using source models from Global CMT for both

earthquakes. We then found the optimum azimuth difference minimizing the root mean square (RMS) misfit between observed and predicted horizontal components at broadband stations used in the present study. The resulting optimum azimuth differences are globally small except for station SNE and FLR that should respectively be rotated by  $-9.3^\circ$  and  $-5.8^\circ$  to fit East and North components of the synthetic waveforms. These values are consistent for both Gorkha and Illapel earthquakes and for different Earth model (we tested the 1D model PREM and a 3D model combining S40RTS and CRUST2.0). We have compared these estimates with the quality control work of Martin Vallée (IPGP, personal communication) to check sensor orientation based on the coherency of teleseismic S-wave arrivals on neighboring stations. Azimuth difference ranges from  $-3^\circ$  to  $-7^\circ$  for SNE, which is slightly smaller than our estimate; and from  $-4^\circ$  to  $-7^\circ$  for FLR, which is consistent with our results. For our waveform inversion, we have rotated horizontal components of SNE and FLR by  $-9.3^\circ$  and  $-5.8^\circ$ , respectively.

#### **Text S4. Tilt time-series**

We used 1 sample/sec records from a tiltmeter located at the summit of the volcano (station SNE in Fig. 1A). The station is composed of two Blum-type pendulum tiltmeters oriented radially and tangentially to the Dolomieu crater. The system operates by measuring the motion of a light spot on a cell with very low instrumental and electronic drifts (Peltier et al., 2016; Toutain et al., 1992). We extracted 800 s time-windows around the origin time of VLP events detected using broadband seismic data. We removed a quadratic trend from these signals and estimated tilt offsets by fitting a function composed of a 2<sup>nd</sup> order polynomial and a simple step function. The resulting signals and tilt steps are shown in Fig. 5B.

#### **Text S5. Moment tensor inversions**

Source inversions were conducted after correcting broadband seismic records to displacement and filtering in the 0.03-0.1 Hz passband. The forward problem can be written as (Aki and Richards, 2002):

$$u_i(\mathbf{x}, \mathbf{t}) = \int M_{pq} S(\tau) G_{ip,q}(\mathbf{x}, \mathbf{t}; \boldsymbol{\xi}, \boldsymbol{\tau}) d\tau$$

where  $u_i(\mathbf{x}, \mathbf{t})$  is the observed displacement at  $(\mathbf{x}, \mathbf{t})$ ,  $G_{ip,q}(\mathbf{x}, \mathbf{t}; \boldsymbol{\xi}, \boldsymbol{\tau})$  is the Earth response to a step function for a source at  $(\boldsymbol{\xi}, \boldsymbol{\tau})$ ,  $M_{pq}$  is the moment tensor and  $S(\tau)$  is a source time function (i.e., proportional to the moment rate). Recently, Legrand and Perton (2022) proposed to model VLP events using quasi-static Green's functions, neglecting inertial terms in the model due to the long-period characteristics of the observed signals. This approach is interesting because it allows to consider complex and finite VLP sources quite easily. However, assuming that the VLP sources can be located anywhere below the central cone, we should consider epicentral distances larger than 4.6 km, corresponding to travel-time delays of  $\sim 1.3$  sec, which is significant compared to the sampling interval of the seismic records (0.01 sec). In addition, as highlighted by Flinders et al. (2020), seismometers only provide a bandpass-filtered version of the true ground motion. To avoid any bias in the source models, we therefore used full Green's functions filtered with the same passband as the recorded data. In practice, we computed  $G_{ip,q}(\mathbf{x}, \mathbf{t}; \boldsymbol{\xi}, \boldsymbol{\tau})$  using the wavenumber

integration method implemented by (Herrmann, 2013) for a local velocity model derived from Battaglia et al. (2005) and the same bandpass filter as the observed waveforms. We inverted for the moment tensor elements of  $M_{pq}$  and the source location  $\xi$  assuming different source-time functions  $S(\tau)$ . After different tests, we found that positive moment-rate functions usually employed for tectonic earthquakes cannot fit the observed waveforms. Instead, we employed a damped oscillating source-time function that has been previously used at other volcanoes to study VLP signals (e.g., Cesca et al., 2020):

$$S(\tau) \propto \exp \frac{-\pi\tau}{QT_R} \sin \frac{2\pi\tau}{T_R}$$

where the resonance period  $T_R$  and the quality factor  $Q$  were estimated by grid-search along with the source location in time and space. For a given source location,  $T_R$  and  $Q$ , the forward problem is linear and the solution to the inverse problem is given by:

$$\mathbf{m} = (\mathbf{G}^T \mathbf{G})^{-1} \mathbf{G}^T \mathbf{d}$$

where  $\mathbf{m}$  is the model vector including the 6 independent elements of the full moment tensor  $\mathbf{d}$  is the data vector including concatenated VLP waveforms and  $\mathbf{G}$  is the so-called Green's function matrix (including Green's functions convolved with the source-time function). This linear inversion was conducted for all explored locations (ranging every 0.005° from -21.26° to -21.24° in latitude, from 55.70° to 55.72° in longitude and from 0.2 km to 1.5 km in depth below the summit), source origin times (ranging from -5s to +15s relative to detection times) and source-time function parameters ( $T_R$  ranging from 10 sec to 22 sec and  $Q$  ranging from 3 to 12). We then selected an optimum solution corresponding to the combination of parameters minimizing the RMS data misfit. Source inversion was conducted by using broadband stations BON, SNE, FJS, FLR, FOR and RVL for which VLP events can be observed. However, to mitigate the impact of long-period noise, we manually rejected records associated with too low signal to noise ratios. Using such approach, we performed source inversion for 24 VLP events out of the 43 events of our catalog. The remaining 19 events were associated with small VLP signals that are visible on too few stations to obtain stable results. However, the similarity of VLP waveforms recorded at the summit (see Fig. S4-S5) suggest that these remaining events have similar source mechanisms. The resonance period of these events were estimated from the spectrum of VLP signals recorded at station SNE (see supplementary Text S6).

To evaluate the compatibility between available observations and different source types, we calculated the RMS misfit associated with various moment tensor source configurations using methodology of Duputel and Rivera (2019) based on the source-type representation introduced by Hudson et al. (1989). The results, presented in Fig. 6B of the main text, indicate that the most favorable source type is close to a tensile crack. We then specifically considered a pure tensile-crack source by enforcing amplitude ratios of  $1:1(\lambda+2\mu)/\lambda$  for the moment tensor eigenvalues (where  $\lambda$  and  $\mu$  are Lame's constants). Assuming a relationship  $\lambda=2\mu$  (corresponding to volcanic rocks close to liquidus; Kumagai, 2022), we found the optimal crack source orientations by testing 2000 random mechanisms uniformly sampled across the focal sphere. Following Duputel and Rivera (2019), the focal mechanism orientation is defined using Euler angles  $\psi$ ,  $\theta$  and  $\phi$

(corresponding respectively to precession, nutation and intrinsic rotations angles). Homogeneous random sampling of the source geometry can be done by using uniform probability distributions for  $\psi$  and  $\varphi$  and a probability distribution  $p(\theta)=\sin(\theta)/2$  for  $\theta$ . We then selected the combination of  $\psi$ ,  $\theta$  and  $\varphi$  that minimize the RMS misfit between data and predictions. Fig. S12 illustrates that imposing a pure crack source does not result in a significant increase in misfit compared to a full moment tensor solution.

We also employed a bootstrap approach to assess the uncertainty associated with the moment tensor solutions. This was done by conducting 100 inversions while randomly generating weighting coefficients for each channel, ensuring that the sum of weights equals the total number of channels. The variability in focal mechanisms is illustrated in Fig. S14 for the VLP event on 24 August 2015 at 19:08:19 UTC by superimposing the deviatoric components of the 100 bootstrapped moment tensor solutions (for a full moment tensor inversion in Fig. S14A and by enforcing a pure tensile crack source Fig. S14B).

### **Text S6. Resonance period of VLP events**

The source inversion outlined in Text S5 enabled the estimation of the resonance period ( $T_R$ ) of VLP events detected at multiple stations. To validate these results and estimate  $T_R$  for small VLP events for which a source model is not available, we additionally measured  $T_R$  using vertical near field records of station SNE.  $T_R$  was determined as the period corresponding to the peak amplitude in the spectrum within the period range of 10 and 100 s (as depicted by dashed lines in the spectra presented in Fig. 8B of the main text). The resulting measurements are shown in Fig. S15. The comparison with moment tensor inversion results reveals differences in  $T_R$  estimates ranging from 0.02 to 1.7 seconds with a standard deviation of 0.8 s.

### **Text S7. Resonance periods of a fluid-filled crack**

At the beginning of the eruption, the VLP events indicated a dike resonance period  $T_R=20$ s. This observation is consistent with the fundamental transverse mode of the dike for which the resonance period can be estimated using (Maeda and Kumagai, 2017):

$$T_R^m = \frac{2W\sqrt{1+2\varepsilon^m C}}{(m-1)a}$$

where  $W$  is the dike width,  $m$  is the mode number,  $a$  is the sound velocity of the magma ( $a = 2$  km/s) and  $\varepsilon^m$  is the constant as defined by (Maeda and Kumagai, 2017):

$$\varepsilon^m = \frac{W}{3mL} \left(1 - 4\gamma \frac{W}{3mL}\right)$$

with  $\gamma=0.22$ . We define  $C$  the crack stiffness,  $C = (b/\mu)(W/d)$  with  $b$  the bulk modulus of the magma and  $\mu$  is the shear modulus of the elastic medium ( $\mu = 14$  GPa from our velocity model). Assuming gas-free basaltic magma with a bulk modulus  $b = 10$  GPa (Huppert and Woods, 2002), this equation predicts a resonance period  $T_R=20$  s for  $m = 2$  when considering a dike length of 2300 m (i.e., the elevation difference between the eruption site and the magma reservoir), a dike thickness  $d = 1$  m and a dike width of  $W = 1440$  m (Dumont et al., 2022).

To analyze the effect of gas content on  $T_R$ , we can then evaluate the bulk modulus of the gas-liquid mixture as:

$$b = \frac{1}{\frac{(1-\phi)}{b_L} + \frac{\phi}{b_G}}$$

where  $\phi$  is the gas volume fraction and  $b_L$  is the bulk modulus of the basaltic liquid (we use  $b_L = 10$  GPa). The gas bulk modulus  $b_G$  can be obtained assuming  $b_G = \gamma \rho g H$ , with  $g = 9.81$  m/s<sup>2</sup>, a depth of  $H = 1$  km (i.e., the VLP centroid depth) and  $\gamma$  the heat capacity ratio (assuming H<sub>2</sub>O,  $\gamma = 1.4$ ). The bulk density of the mixture is given by  $\rho = (1 - \phi)\rho_L + \phi\rho_G$  where  $\rho_L$  is the density of the liquid,  $\rho_G$  is the gas density. The sound velocity of the gas-liquid mixture can then be estimated using  $a = \sqrt{b/\rho}$ . As shown in Fig. S16, increasing the gas content reduces the resonance period  $T_R$ . However, the observed variation from  $T_R=20$  s at the onset of the eruption to  $T_R=13$  s at the end of the eruption would correspond to an unrealistic variation of the magma gas volume fraction (from 100% at the beginning of the eruption to 0% at the end of the eruption). We then investigated the variation of the resonance period  $T_R$  as a function of the dike width. To simplify our interpretation, we considered relative changes in dike width, that is:

$$\frac{\delta W}{W} = \frac{W(T_R) - W(T_R = 20 \text{ sec})}{W(T_R = 20 \text{ sec})}$$

where  $W(T_R)$  is the crack width corresponding to a resonance period  $T_R$  (we assumed  $T_R = 20$  sec at the beginning of the eruption). As illustrated in Fig S19, investigating changes of  $T_R$  with respect to  $\delta W/W$  mitigates any dependency on the mode number, dike length and dike thickness. The variation of  $T_R$  in Fig. 9 is therefore valid for any mode and for any dike length and thickness.

To investigate the effect of viscous flow that is not accounted for in the equations above, we also used the model of Lipovsky and Dunham (2015). Specifically, we employed the closed form expressions for the resonance period ( $T_R$ ) and quality factor ( $Q$ ) of the fundamental mode in the boundary layer crack wave limit to estimate the dike width ( $W$ ) and magma viscosity ( $\nu$ ):

$$W = \frac{1}{2} \left[ \frac{\pi \nu}{\rho} \left( \frac{\mu}{(1 - v_s)} \right)^2 Q^2 T_R^5 \right]^{1/6}$$

$$\nu = \frac{4 \pi \rho h^2}{Q^2 T_R}$$

where  $h$  is the half thickness of the dike. The results presented in Fig. S20 were obtained assuming  $\rho=2500$  kg/m<sup>3</sup>,  $\mu=14$  GPa (as considered in Fig. 9 and S19),  $v_s=0.25$  (as in Text S5) and  $h=1$  m. The results are globally consistent with results based on Maeda and Kumagai (2017) with a ~20% reduction in the dike width from 1300 m to 1000 m during the second VLP swarm. There is an overall increase in magma viscosity towards the end of the eruption with values around 200 to 400 Pa.s, consistent with previous estimates at Piton de la Fournaise volcano (Harris et al., 2019; Kolzenburg et al., 2019; Lipovsky and Dunham, 2015; Rhéty et al., 2017; Villeneuve et al., 2008).

### **Text S8. Gas volume fraction at Piton de la Fournaise**

To have an order of magnitude of gas volume fraction at Piton de la Fournaise, we used the following relationship (Villemant and Boudon, 1998):

$$\phi = \frac{K_R (X_i - X_{H_2O})}{P}$$

where  $K_R$  is a constant,  $X_{H_2O}$  is the content of  $H_2O$  (wt%) at pressure  $P$  in the dike (in MPa) and  $X_i$  is the initial water content (when  $P$  is larger than the saturation pressure). Here, we only considered  $H_2O$  as it is the dominant volatile component at Piton de la Fournaise (Allard, P. et al., 2011; Lénaït et al., 1989). We used  $K_R = 15$  corresponding to a temperature  $T = 1100^\circ\text{C}$  and a magma density  $\rho = 2500 \text{ kg/m}^3$ . We estimated  $X_{H_2O}$  using the empirical relationship proposed by (Muro et al., 2016) at Piton de la Fournaise:

$$X_{H_2O} = 0.1759 \ln(P) + 4.019 \cdot 10^{-31} \ln(0.0556 \cdot T) + 0.1640$$

We show the corresponding evolution of the gas volume fraction  $\phi$  as a function of pressure  $P$  and depth in Fig. S17. The vapor content is expected to be negligible when going to depths larger than a few hundreds of meters.

### **Movie S1.**

Time-lapse movie showing the onset of the August-October 2015 eruption from camera station BERC (looking north-northeast from the south of the terminal cone, location of the station shown in Fig. 1).

### **Movie S2.**

Time-lapse movie showing the onset of the August-October 2015 eruption from camera station BASC (looking south-east from the north-west of the terminal cone, location of the station shown in Fig. 1).

### **References**

- Aki, K., Richards, P.G., 2002. Quantitative Seismology, 2nd ed. University Science Books, Sausalito, CA.
- Allard, P., La Spina, A., Tamburello, G., Aiuppa, A., Muro, A. D., Staudacher, T., 2011. First Measurements of Magmatic Gas Composition and FLuxes during an Eruption (October 2010) of Piton de La Fournaise Hot Spot Volcano, La Reunion Island, Geophysical Research Abstracts 13, EGU2011-13182. Geophysical Research Abstracts, EGU General Assembly GMPV5, 13182.
- Battaglia, J., Ferrazzini, V., Staudacher, T., Aki, K., Cheminée, J.-L., 2005. Pre-eruptive migration of earthquakes at the Piton de la Fournaise volcano (Réunion Island). Geophys. J. Int. 161, 549–558. <https://doi.org/10.1111/j.1365-246X.2005.02606.x>
- Beauducel, F., Lafon, D., Béguin, X., Saurel, J.-M., Bosson, A., Mallarino, D., Boissier, P., Brunet, C., Lemarchand, A., Anténor-Habazac, C., Nercessian, A., Fahmi, A.A., 2020a.

- WebObs: The Volcano Observatories Missing Link Between Research and Real-Time Monitoring. *Front. Earth Sci.* 8. <https://doi.org/10.3389/feart.2020.00048>
- Beauducel, F., Peltier, A., Villié, A., Suryanto, W., 2020b. Mechanical Imaging of a Volcano Plumbing System From GNSS Unsupervised Modeling. *Geophys. Res. Lett.* 47, e2020GL089419. <https://doi.org/10.1029/2020GL089419>
- Cesca, S., Letort, J., Razafindrakoto, H.N.T., Heimann, S., Rivalta, E., Isken, M.P., Nikkhoo, M., Passarelli, L., Petersen, G.M., Cotton, F., Dahm, T., 2020. Drainage of a deep magma reservoir near Mayotte inferred from seismicity and deformation. *Nature Geosci.* 13, 87–93. <https://doi.org/10.1038/s41561-019-0505-5>
- Dumont, Q., Cayol, V., Froger, J.-L., Peltier, A., 2022. 22 years of satellite imagery reveal a major destabilization structure at Piton de la Fournaise. *Nat Commun* 13, 2649. <https://doi.org/10.1038/s41467-022-30109-w>
- Duputel, Z., Lengliné, O., Ferrazzini, V., 2019. Constraining Spatiotemporal Characteristics of Magma Migration at Piton De La Fournaise Volcano From Pre-eruptive Seismicity. *Geophys. Res. Lett.* 46, 119–127. <https://doi.org/10.1029/2018GL080895>
- Duputel, Z., Rivera, L., 2019. The 2007 caldera collapse of Piton de la Fournaise volcano: Source process from very-long-period seismic signals. *Earth Planet. Sci. Lett.* 527, 115786. <https://doi.org/10.1016/j.epsl.2019.115786>
- Flinders, A.F., Johanson, I.A., Dawson, P.B., Anderson, Kyle R., Haney, Matthew M., Shiro, Brian R., 2020. Very-Long-Period (VLP) Seismic Artifacts during the 2018 Caldera Collapse at Kīlauea, Hawai‘i | Seismological Research Letters | GeoScienceWorld. *Seismological Research Letters* 91, 3417–3432. <https://doi.org/10.1785/0220200083>
- Harris, A., Mannini, S., Thivet, S., Chevrel, M.O., Gurioli, L., Villeneuve, N., Di Muro, A., Peltier, A., 2019. How shear helps lava to flow. *Geology* 48, 154–158. <https://doi.org/10.1130/G47110.1>
- Herring, T. A., King, R. W., McClusky, S. C., 2010. GPS analysis at MIT, Release 10.4.
- Herrmann, R.B., 2013. Computer Programs in Seismology: An Evolving Tool for Instruction and Research. *Seismol. Res. Lett.* 84, 1081–1088. <https://doi.org/10.1785/0220110096>
- Hudson, J.A., Pearce, R.G., Rogers, R.M., 1989. Source type plot for inversion of the moment tensor. *Journal of Geophysical Research: Solid Earth (1978–2012)* 94, 765–774. <https://doi.org/10.1029/JB094iB01p00765>
- Huppert, H.E., Woods, A.W., 2002. The role of volatiles in magma chamber dynamics. *Nature* 420, 493–495. <https://doi.org/10.1038/nature01211>
- Kolzenburg, S., Giordano, D., Muro, A.D., Dingwell, D.B., 2019. Equilibrium Viscosity and Disequilibrium Rheology of a high Magnesium Basalt from Piton De La Fournaise volcano, La Reunion, Indian Ocean, France. *Annals of Geophysics* 62, VO218–VO218. <https://doi.org/10.4401/ag-7839>
- Kumagai, H., 2022. Source Quantification of Volcanic-Seismic Signals, in: Tilling, R.I. (Ed.), . Springer US, New York, NY, pp. 425–467.
- Legrand, D., Perton, M., 2022. What are VLP signals at Stromboli volcano? *J. Volc. Geoth. Res.* 421, 107438. <https://doi.org/10.1016/j.jvolgeores.2021.107438>
- Lénat, J.-F., Bachèlery, P., Bonneville, A., Tarits, P., Cheminée, J.-L., Delorme, H., 1989. The December 4, 1983 to February 18, 1984 eruption of Piton de la Fournaise (La Reunion, Indian Ocean): Description and interpretation. *J. Volc. Geoth. Res.* 36, 87–112. [https://doi.org/10.1016/0377-0273\(89\)90007-3](https://doi.org/10.1016/0377-0273(89)90007-3)

- Lengliné, O., Duputel, Z., Ferrazzini, V., 2016. Uncovering the hidden signature of a magmatic recharge at Piton de la Fournaise volcano using small earthquakes. *Geophys. Res. Lett.* 43, 4255–4262. <https://doi.org/10.1002/2016GL068383>
- Lipovsky, B.P., Dunham, E.M., 2015. Vibrational modes of hydraulic fractures: Inference of fracture geometry from resonant frequencies and attenuation. *Journal of Geophysical Research: Solid Earth* 120, 1080–1107. <https://doi.org/10.1002/2014JB011286>
- Maeda, Y., Kumagai, H., 2017. A generalized equation for the resonance frequencies of a fluid-filled crack. *Geophys. J. Int.* 209, 192–201. <https://doi.org/10.1093/gji/ggx019>
- Muro, A.D., Métrich, N., Allard, P., Aiuppa, A., Burton, M., Galle, B., Staudacher, T., 2016. Magma Degassing at Piton de la Fournaise Volcano, in: *Active Volcanoes of the Southwest Indian Ocean*. Springer, pp. 203–222.
- Nikkhoo, M., Walter, T.R., Lundgren, P.R., Prats-Iraola, P., 2017. Compound dislocation models (CDMs) for volcano deformation analyses. *Geophys. J. Int.* 208, 877–894. <https://doi.org/10.1093/gji/ggw427>
- Peltier, A., Beauducel, F., Staudacher, T., Catherine, P., Kowalski, P., 2016. Contribution of Tiltmeters and Extensometers to Monitor Piton de la Fournaise Activity, in: Bachelery, P., Lenat, J.-F., Di Muro, A., Michon, L. (Eds.), *Active Volcanoes of the Southwest Indian Ocean, Active Volcanoes of the World*. Springer Berlin Heidelberg, Berlin, Heidelberg, pp. 287–303. [https://doi.org/10.1007/978-3-642-31395-0\\_17](https://doi.org/10.1007/978-3-642-31395-0_17)
- Rhétty, M., Harris, A., Villeneuve, N., Gurioli, L., Médard, E., Chevrel, O., Bachéléry, P., 2017. A comparison of cooling-limited and volume-limited flow systems: Examples from channels in the Piton de la Fournaise April 2007 lava-flow field. *Geochemistry, Geophysics, Geosystems* 18, 3270–3291. <https://doi.org/10.1002/2017GC006839>
- Toutain, J.-P., Bachelery, P., Blum, P.-A., Cheminee, J.-L., Delorme, H., Fontaine, L., Kowalski, P., Taochy, P., 1992. Real time monitoring of vertical ground deformations during eruptions at Piton de la Fournaise. *Geophys. Res. Lett.* 19, 553–556. <https://doi.org/10.1029/91GL00438>
- Villemant, B., Boudon, G., 1998. Transition from dome-forming to plinian eruptive styles controlled by H<sub>2</sub>O and Cl degassing. *Nature* 392, 65–69. <https://doi.org/10.1038/32144>
- Villeneuve, N., Neuville, D.R., Boivin, P., Bachélery, P., Richet, P., 2008. Magma crystallization and viscosity: A study of molten basalts from the Piton de la Fournaise volcano (La Réunion island). *Chemical Geology*, 8th Silicate Melt Workshop 256, 242–251. <https://doi.org/10.1016/j.chemgeo.2008.06.039>
- Waldhauser, F., Ellsworth, W.L., 2000. A Double-Difference Earthquake Location Algorithm: Method and Application to the Northern Hayward Fault, California. *Bull. Seism. Soc. Am.* 90, 1353–1368. <https://doi.org/10.1785/0120000006>
- Zumberge, J.F., Heflin, M.B., Jefferson, D.C., Watkins, M.M., Webb, F.H., 1997. Precise point positioning for the efficient and robust analysis of GPS data from large networks. *Earth Space Sci.* 102, 5005–5017. <https://doi.org/10.1029/96JB03860>

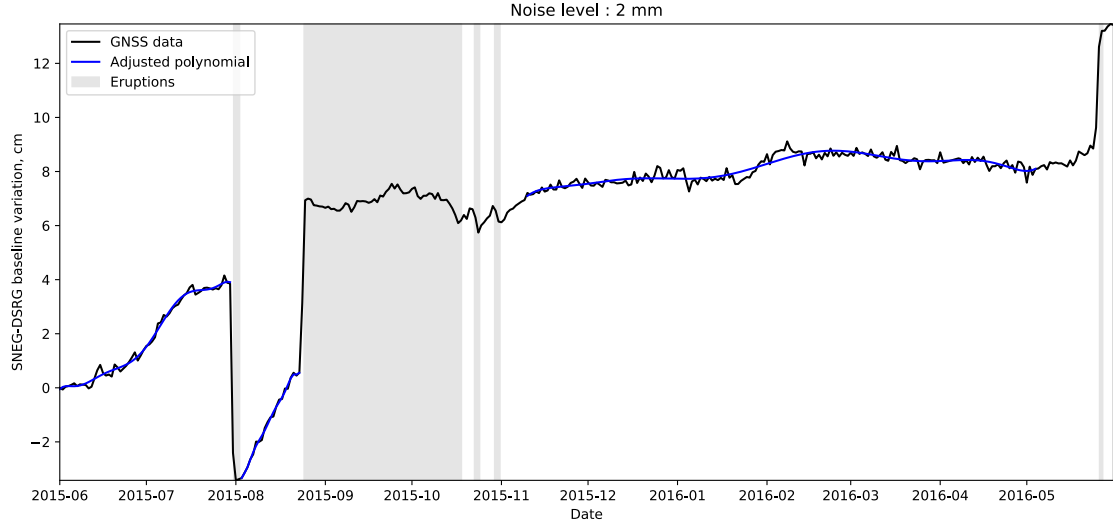


**Fig. S1. Estimating noise level in SNEG-DSRG baseline variations.** As detailed in Text S2, we compute the standard deviation of the residuals between the baseline time-series (in black) and a polynomial fit (in blue) during inter-eruptive time-periods. Grey area indicate eruptions.

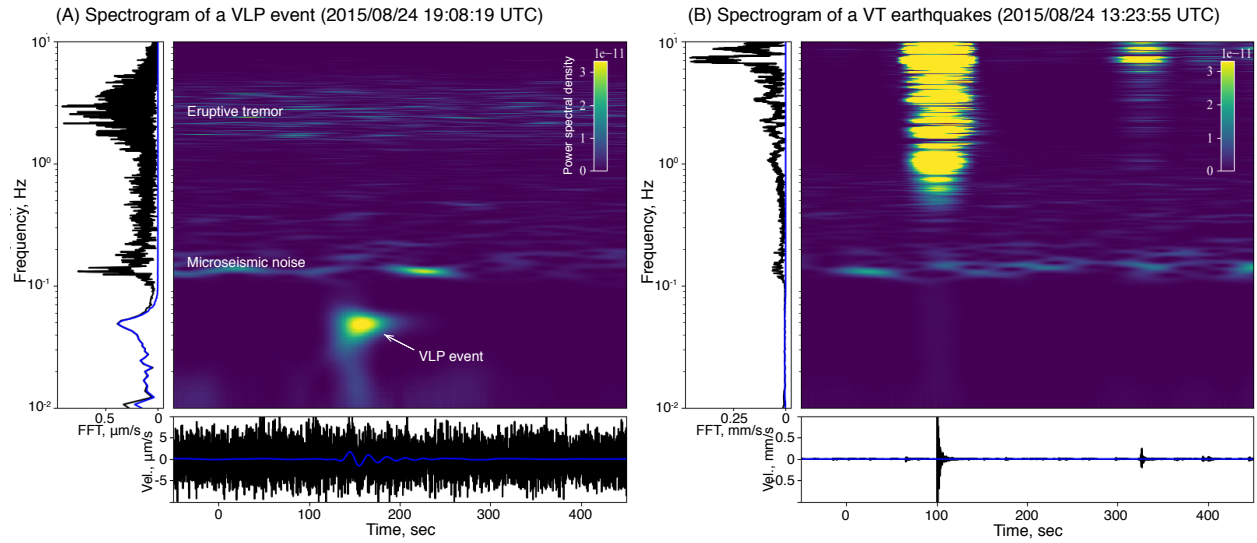


**Fig. S2. Comparison of VLP and VT events at station SNE.** **(A)** Spectrogram of a VLP event (same as Fig. 4A in the main text). Bottom subfigure shows the seismogram and Left plot show the amplitude spectrum. Black lines correspond to the raw ground velocity record while blue lines are filtered in the 0.01-0.07 Hz passband. **(B)** Spectrogram of Volcano-Tectonic (VT) events during the seismic swarm that preceded the August-October 2015 eruption at Piton de la Fournaise. Although the record shown in (B) includes many VT events (more than 30 earthquakes have been detected in this time-window), it is dominated by a large VT around 100 sec with a duration magnitude  $M_d=2.7$  and a smaller one around 330 sec with a magnitude  $M_d=1.2$ . Note that the color scales of (A) and (B) are the same, but the spectrums on the left and seismograms on the bottom have a different scale.

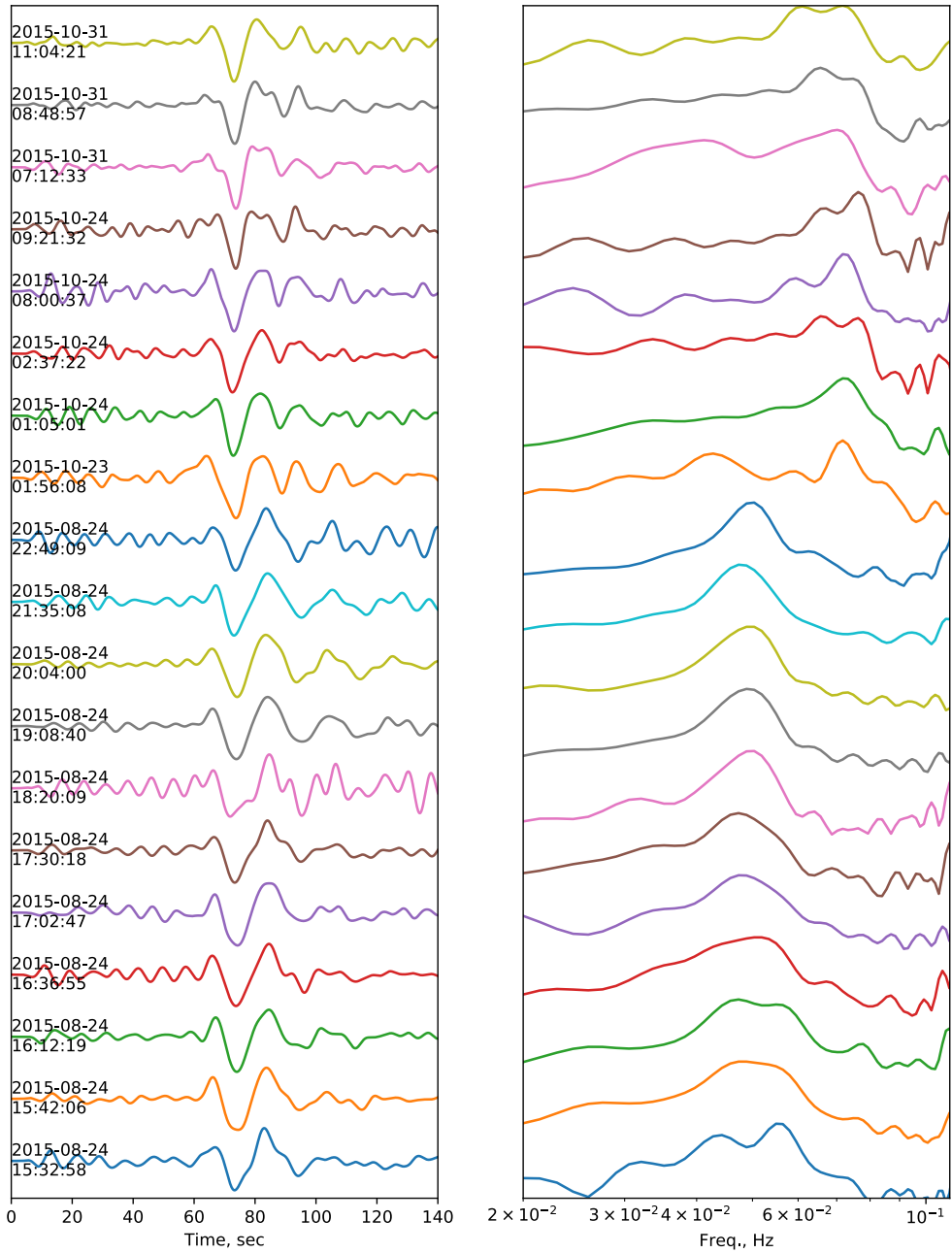


**Fig. S3. VLP templates.** We show template waveforms recorded on the vertical component of station SNE (left) and the corresponding amplitude spectra (right). The time in the left subplot is given with reference to the time stamp indicated on the left of each waveform.

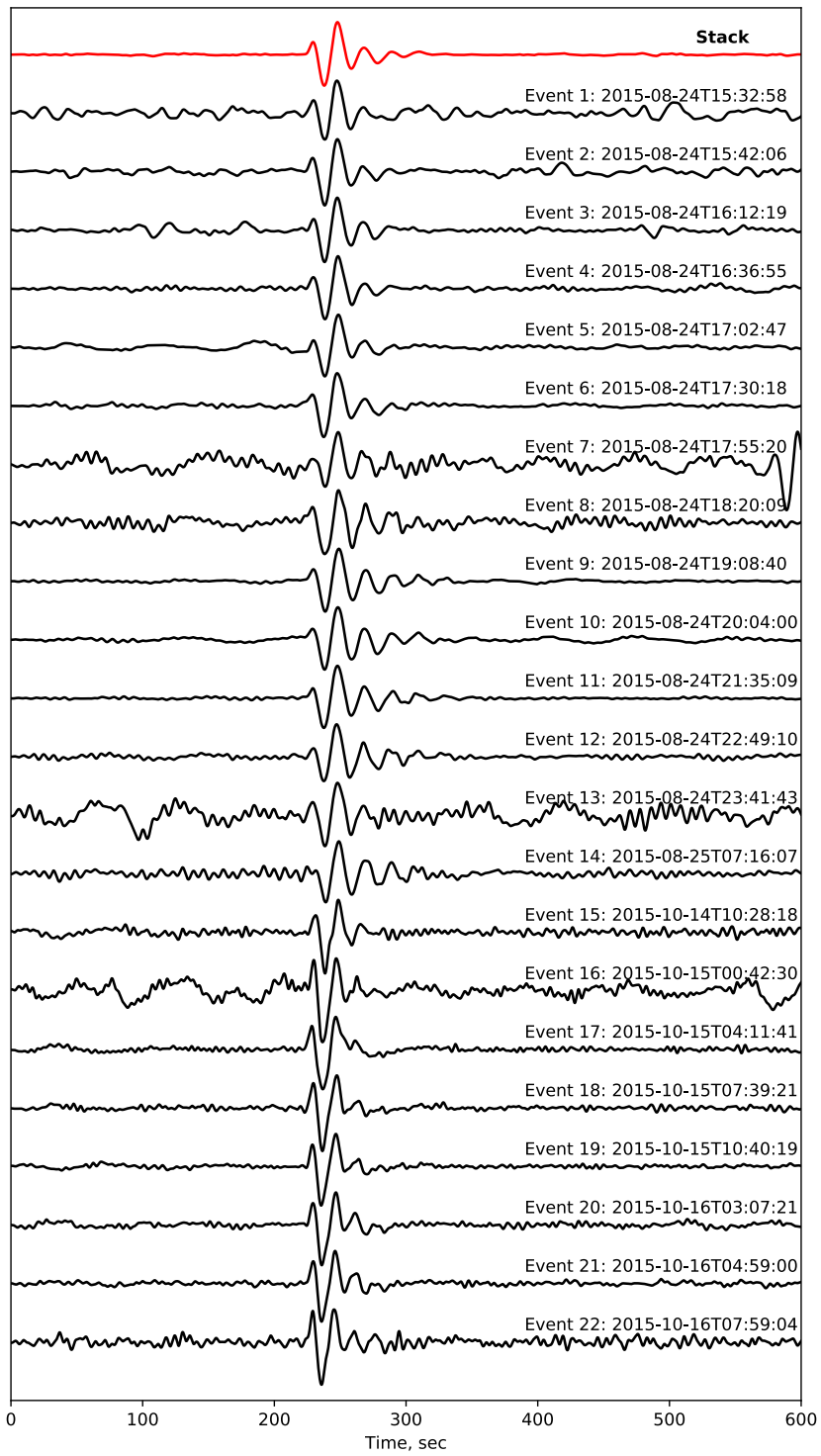


**Fig. S4. VLP events 1 to 22 recorded on the vertical component of station SNE.** Data is bandpass filtered between 0.01 and 0.07Hz. The event number and detection time are indicated on the right side of each trace. The top red trace is the stack of the waveforms shown below.

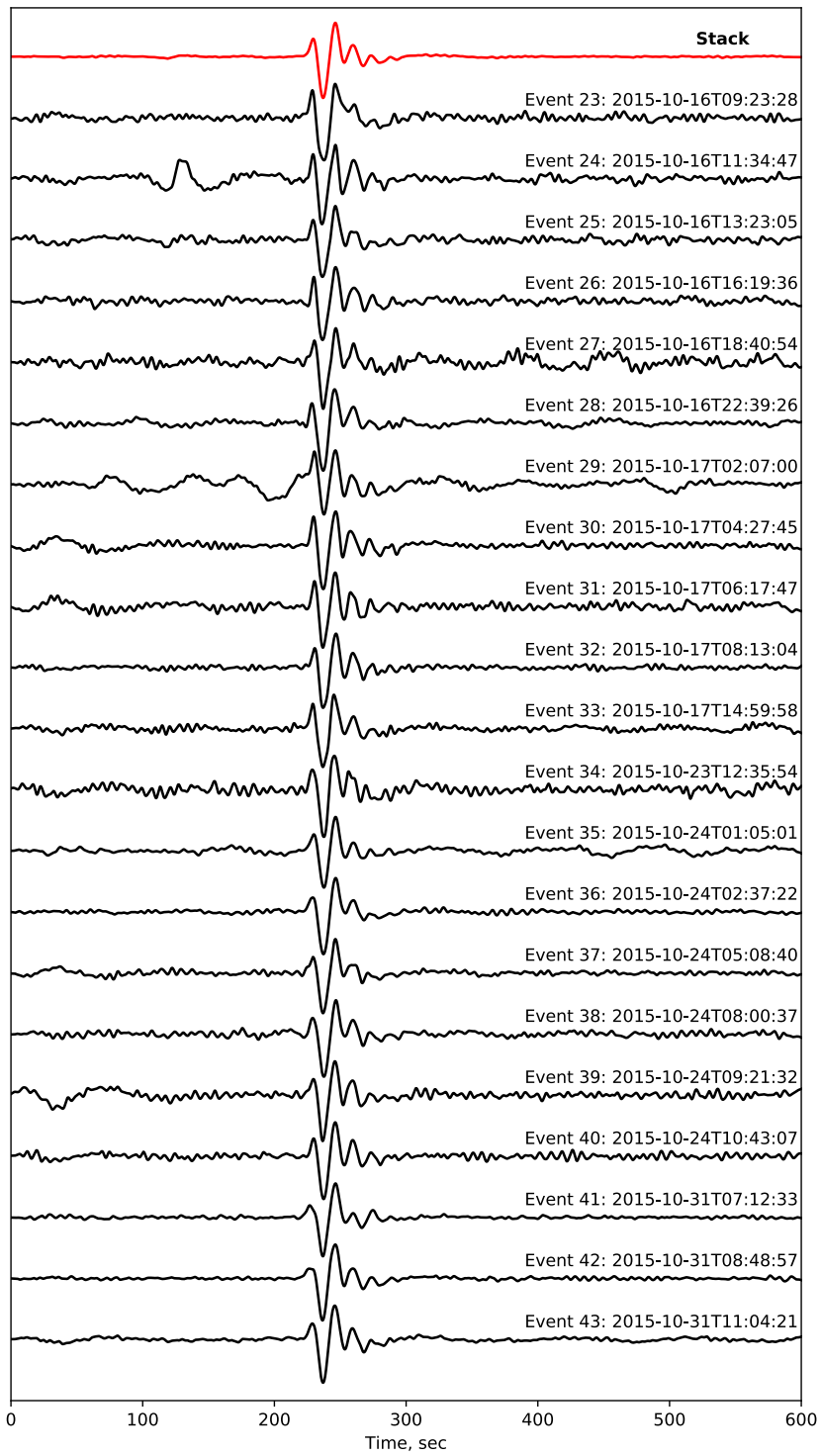


**Fig. S5. VLP events 23 to 43 recorded on the vertical component of station SNE.** Data is bandpass filtered between 0.01 and 0.07Hz. The event number and detection time are indicated on the right side of each trace. The top red trace is the stack of waveforms shown below.

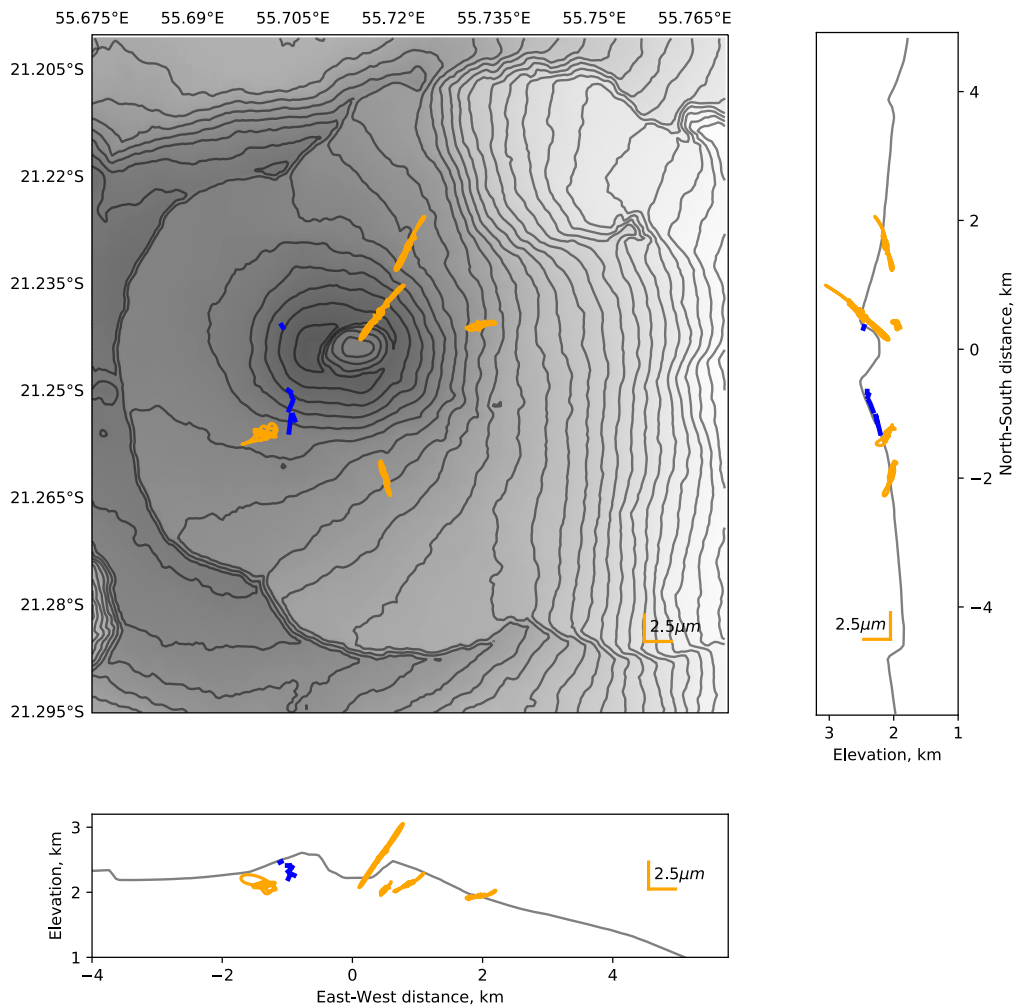


**Fig. S6. Example of particle motions for VLP event 1** (2015-08-24T15:32:58 UTC) shown in orange in map view, East-West and North-South cross-sections. Blue lines indicate the location of eruptive fissures.

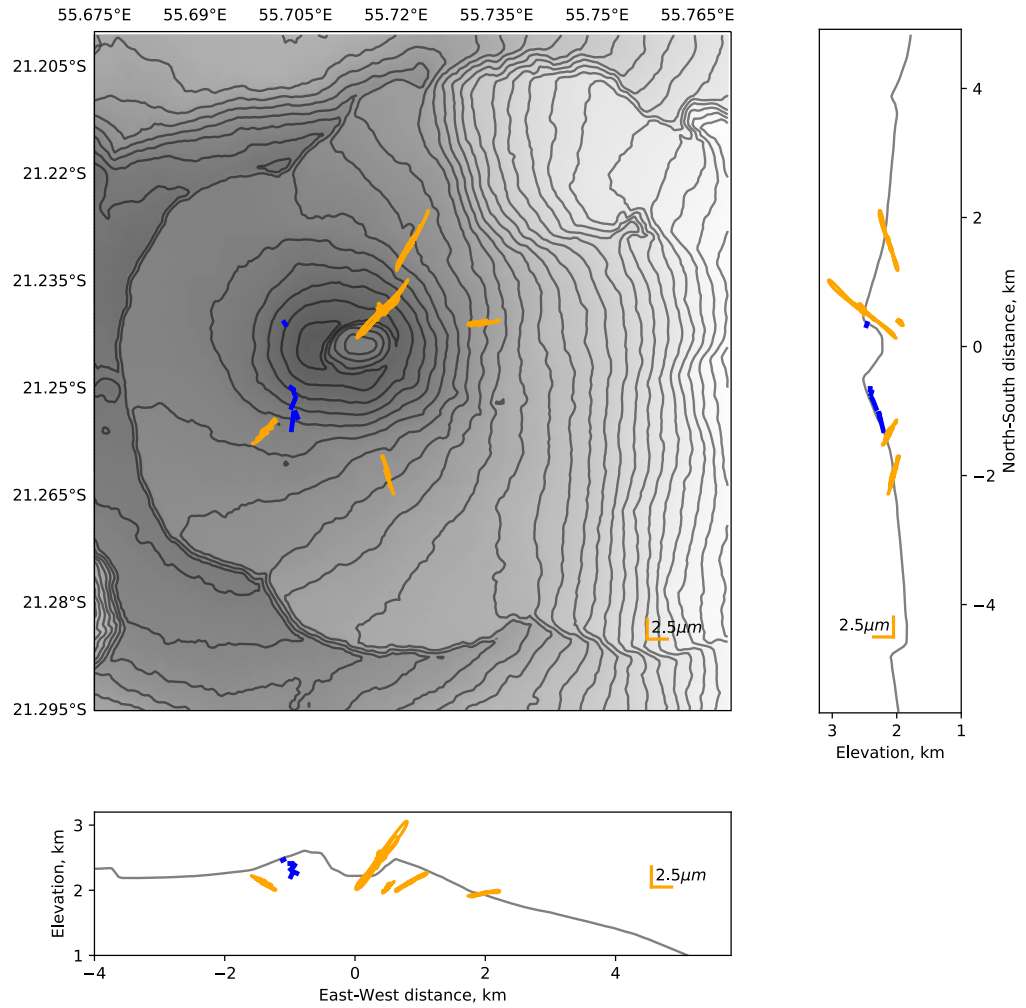


**Fig. S7. Example of particle motions for VLP event 10** (2015-08-24T16:36:55 UTC) shown in orange in map view, East-West and North-South cross-sections. Blue lines indicate the location of eruptive fissures.

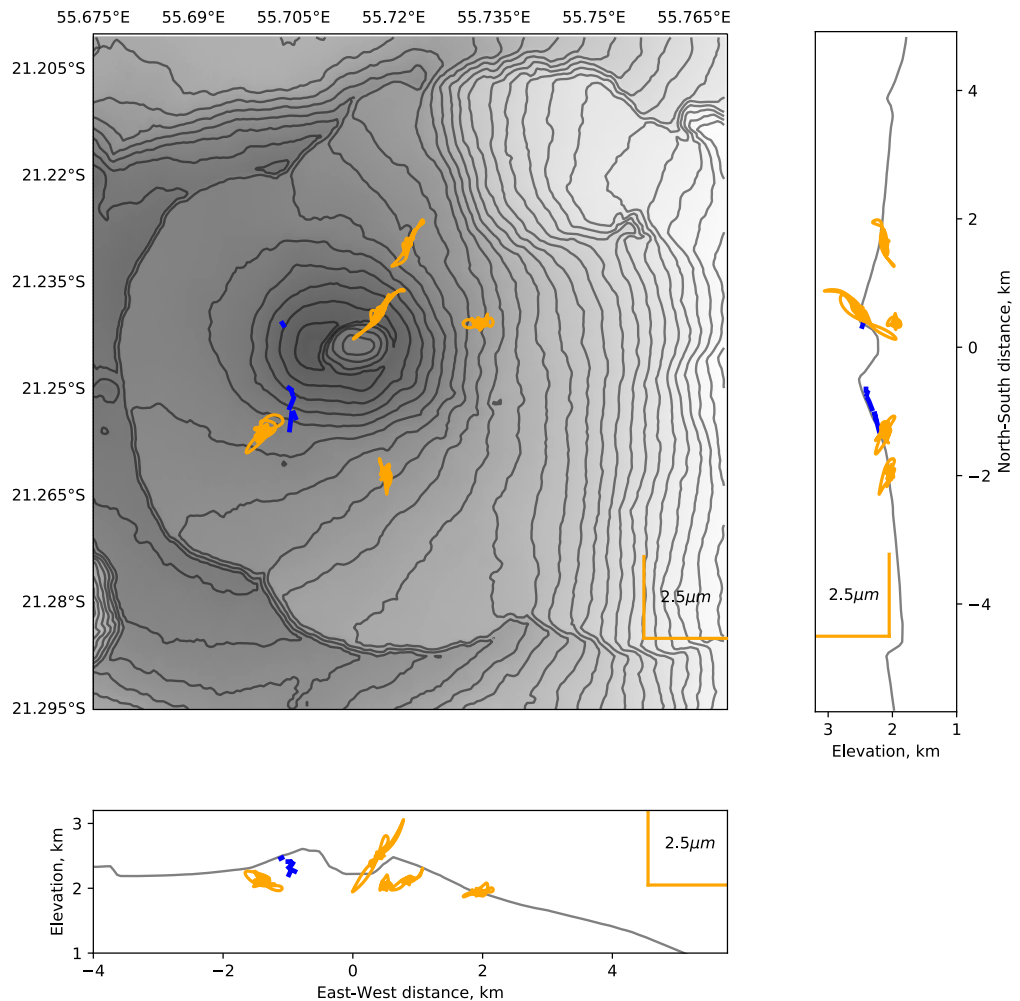


**Fig. S8. Example of particle motions for VLP event 33 (2015-10-17T14:59:58 UTC)** shown in orange in map view, East-West and North-South cross-sections. Blue lines indicate the location of eruptive fissures.

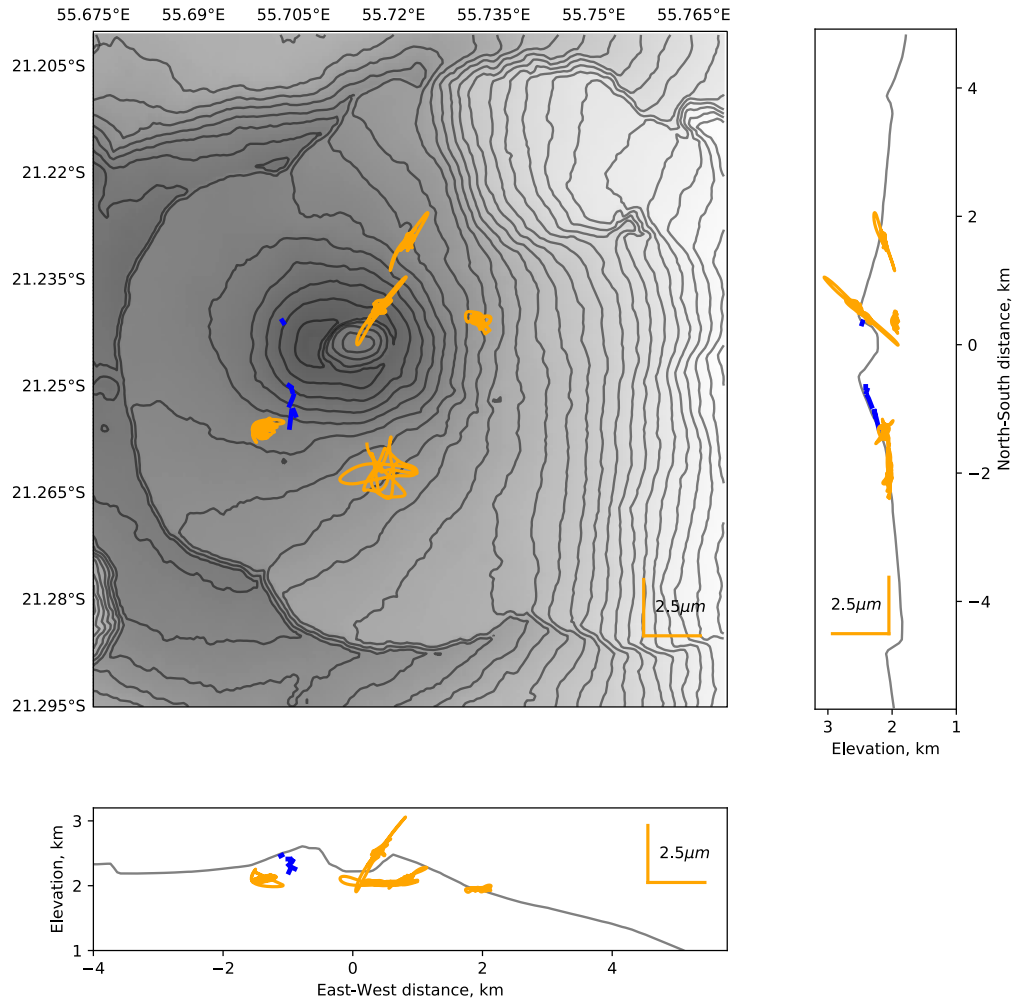


**Fig. S9. Example of particle motions for VLP event 36** (2015-10-24T02:37:22 UTC) shown in orange in map view, East-West and North-South cross-sections. Blue lines indicate the location of eruptive fissures.

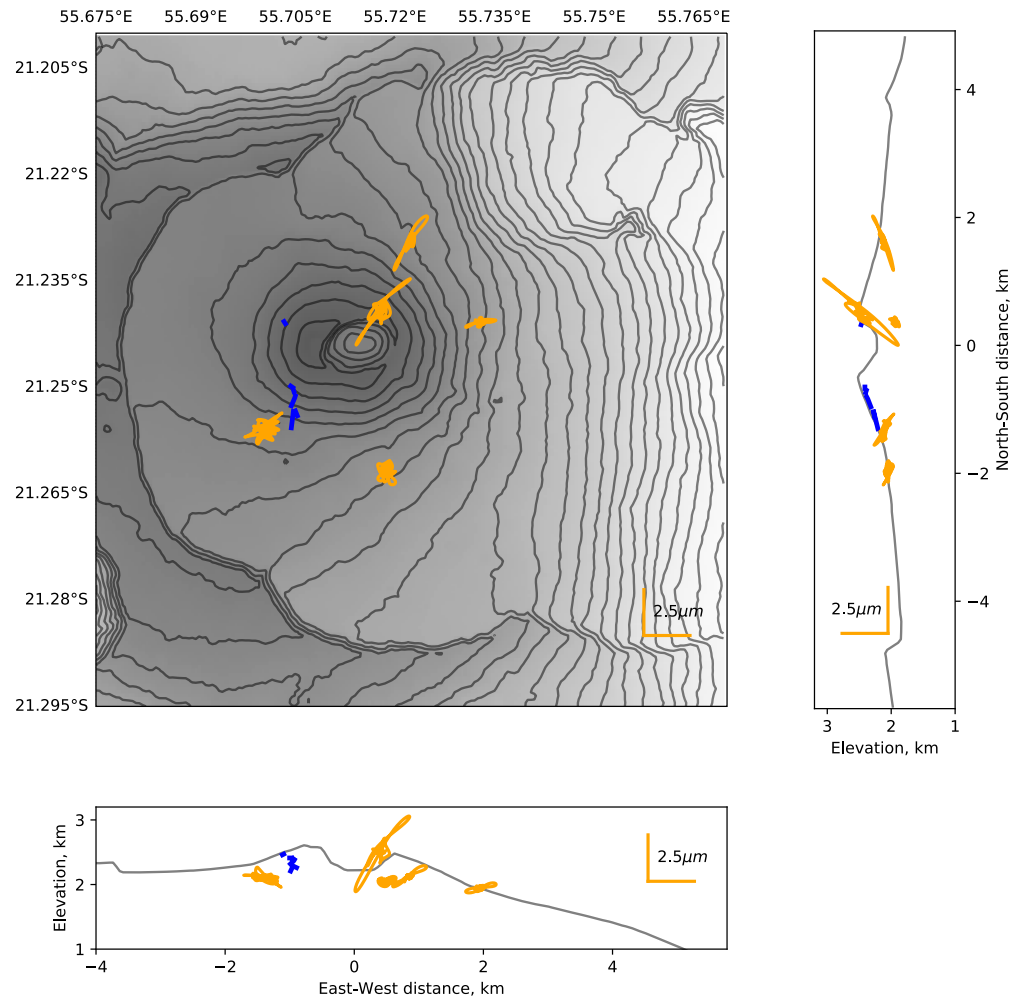


**Fig. S10. Example of particle motions for VLP event 43** (2015-10-31T11:04:21 UTC) shown in orange in map view, East-West and North-South cross-sections. Blue lines indicate the location of eruptive fissures.

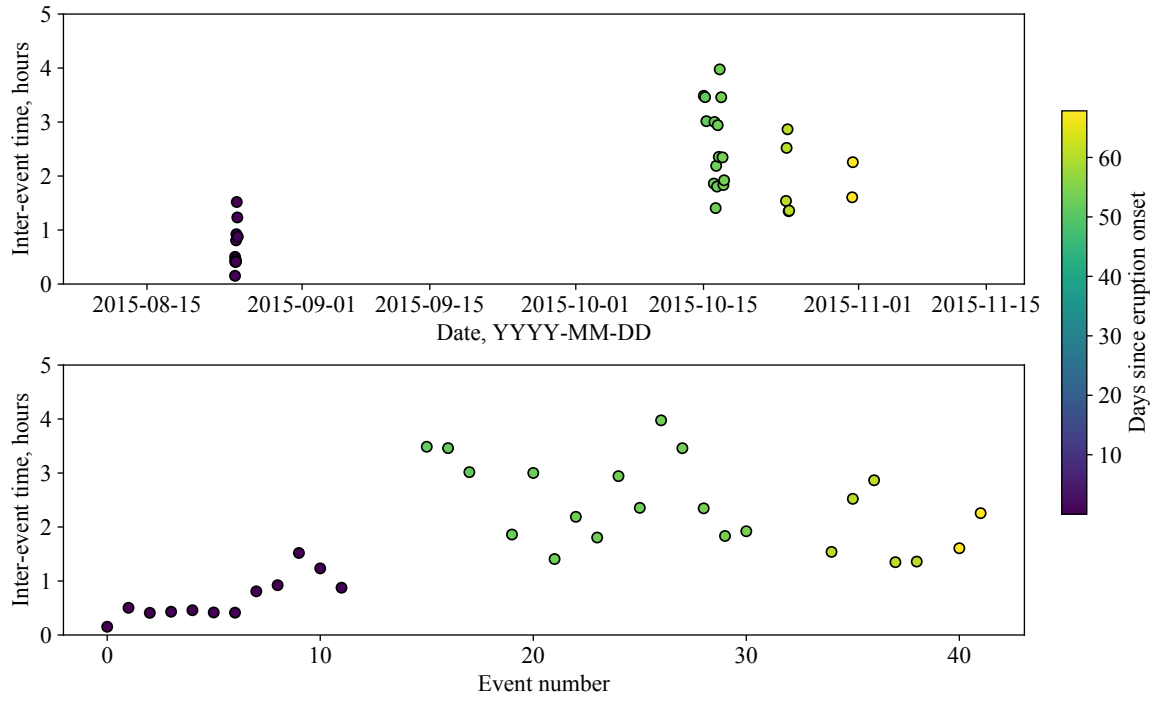
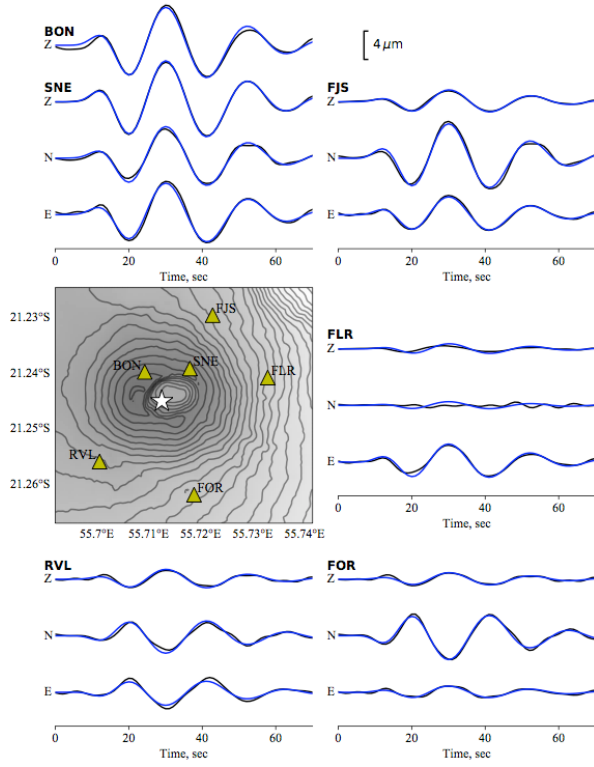


**Fig. S11. Time-evolution of VLP inter-event time.** Notice that we changed the Y-axis limits to focus on inter-ervent times during each swarm (large inter-event delays are observed between the last and first VLP events of each swarm).

(A) Waveform fit for a full Moment tensor inversion



(B) Waveform for a tensile crack source inversion

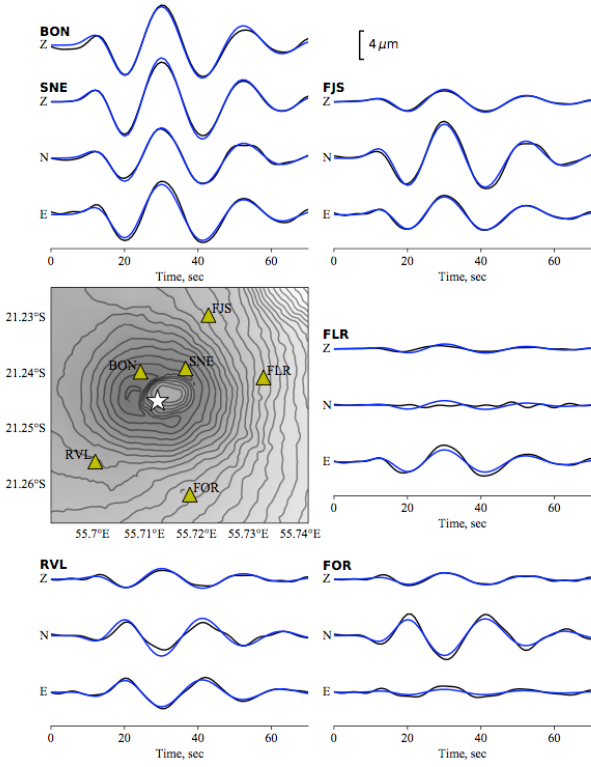


**Fig. S12. Data fit for different source parameterization of VLP event 9 (2015-08-24T19:08:40 UTC).** (A) Comparison between observed (black) and predicted (red) waveforms for a full moment tensor inversion. (B) Waveform fit assuming a pure crack source.

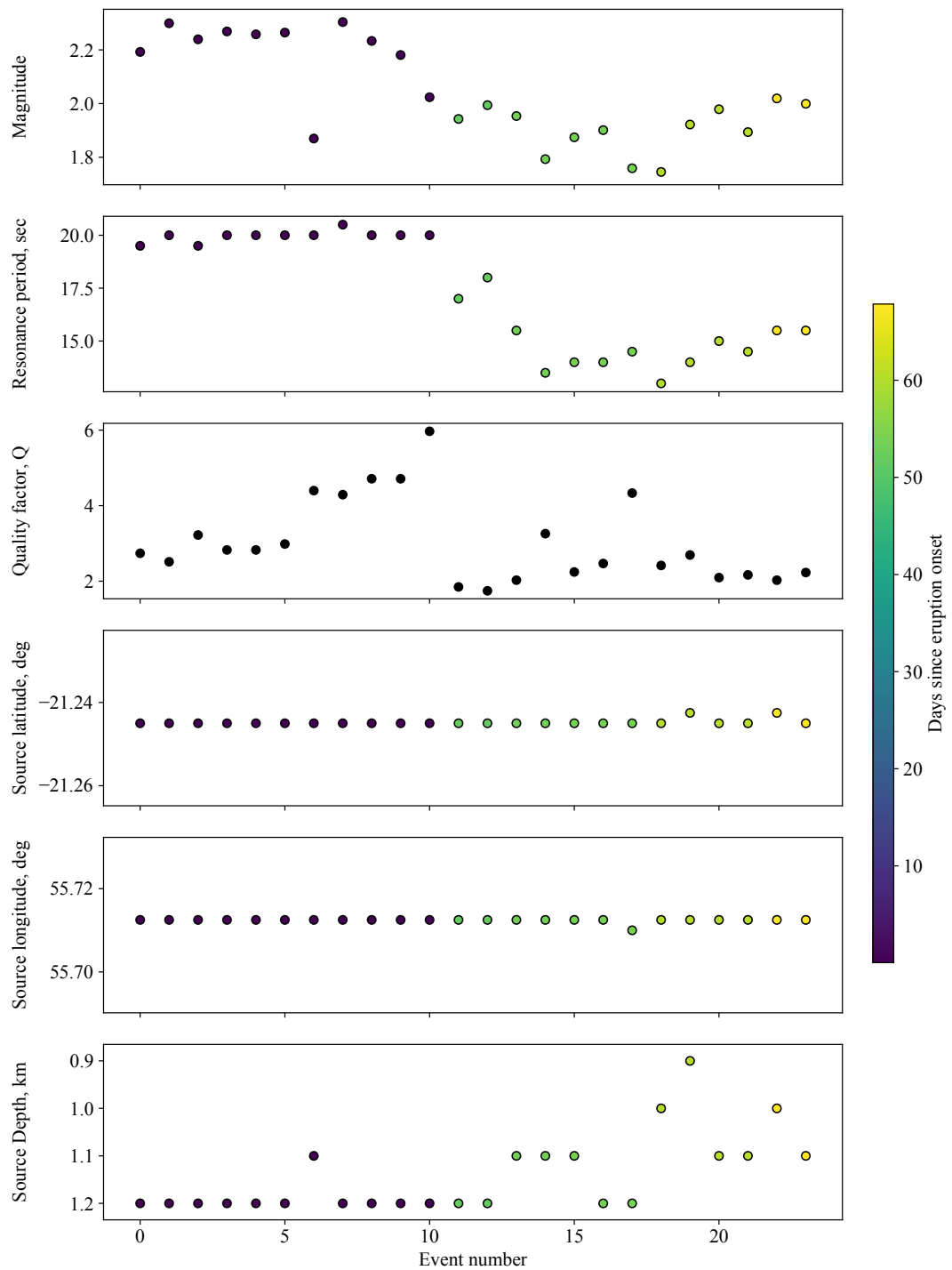
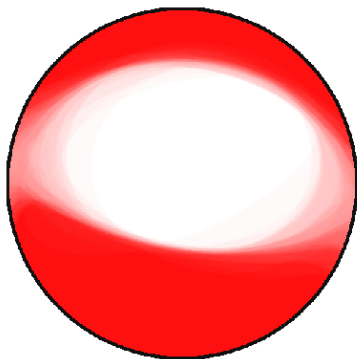


**Fig. S13. Time-evolution of VLP source parameters.** This figure shows source parameters estimated from CMT inversion of VLP signals. Colors indicate the time in days since the eruption onset (on August 24, 2015).

(A) Bootstrap results - Full MT inversion



(B) Bootstrap results - Crack source inversion

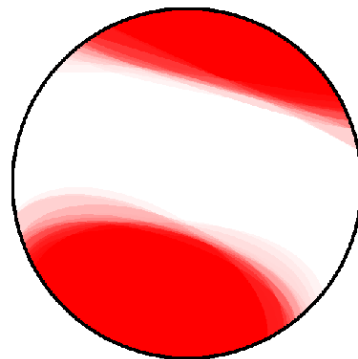


**Fig. S14. Bootstrap analysis of the VLP event on 24 August 2015 at 19:08:19 UTC.** We only show the deviatoric part of the moment tensor solution to show the uncertainty on the focal mechanism orientation. (A) Bootstrap results for the full moment tensor solution. (B) Bootstrap result for a pure crack source. The bootstrap analysis is described in the Text S5.

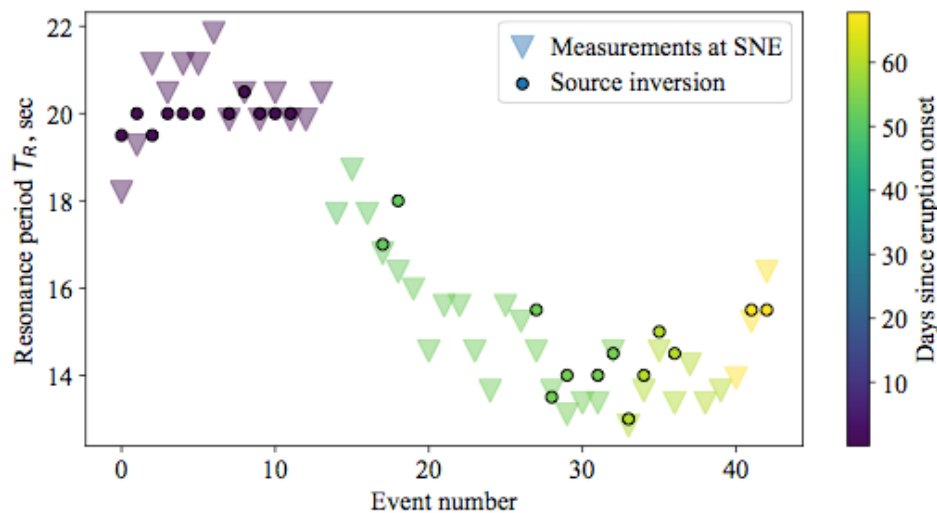


**Fig. S15. VLP resonance period ( $T_R$ ) estimates.** We compare estimates from the source inversion results (circles, Text S5) and  $T_R$  determined from the peak spectral amplitude of station SNE (triangles, Text S6). Measurements are ordered chronologically as a function of the VLP event number and color-coded as a function of the number of days since the eruption onset.

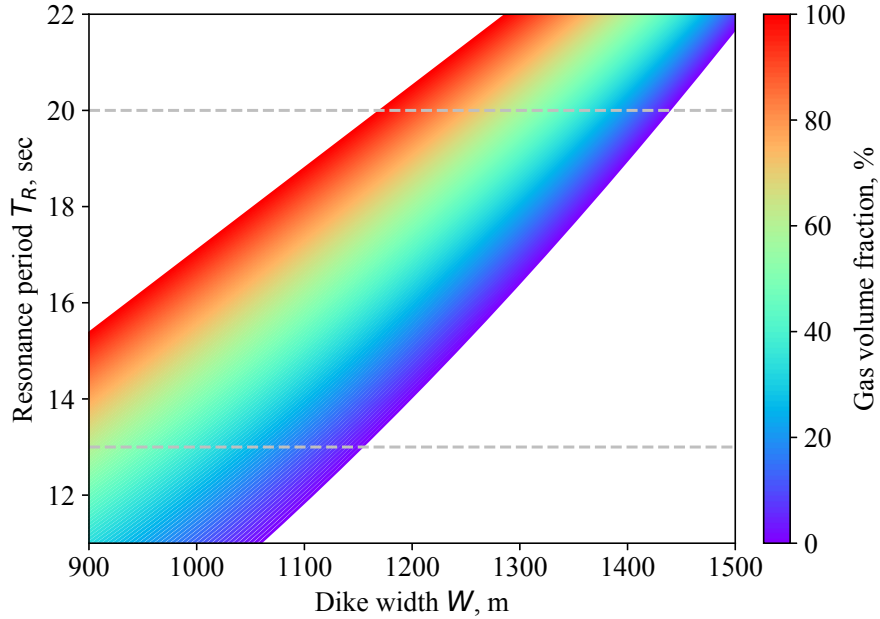


**Fig. S16. Resonance period as a function of the dike width and gas volume fraction.** We assume a transverse mode  $m=2$  and a dike length  $L=2300$  m (see supplementary Text S7). Horizontal dashed grey lines indicate the resonance periods  $T_R = 20$  sec and  $T_R = 13$  sec, observed at the beginning and at the end of the sequence, respectively.

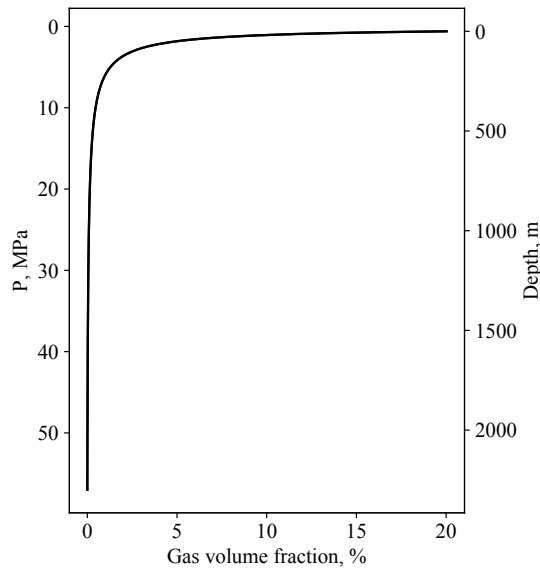


**Fig. S17. Magma gas volume fraction  $\phi$  as a function of pressure and depth.**  $\phi$  is derived using previous analyzes of dissolved  $H_2O$  in glass inclusions and matrices at Piton de la Fournaise (see supplementary Text S8). Pressure  $P$  at various depths is estimated assuming magmastic pressure, an overpressure of  $5 \cdot 10^5$  Pa in the dike and an atmospheric pressure of  $10^5$  Pa.

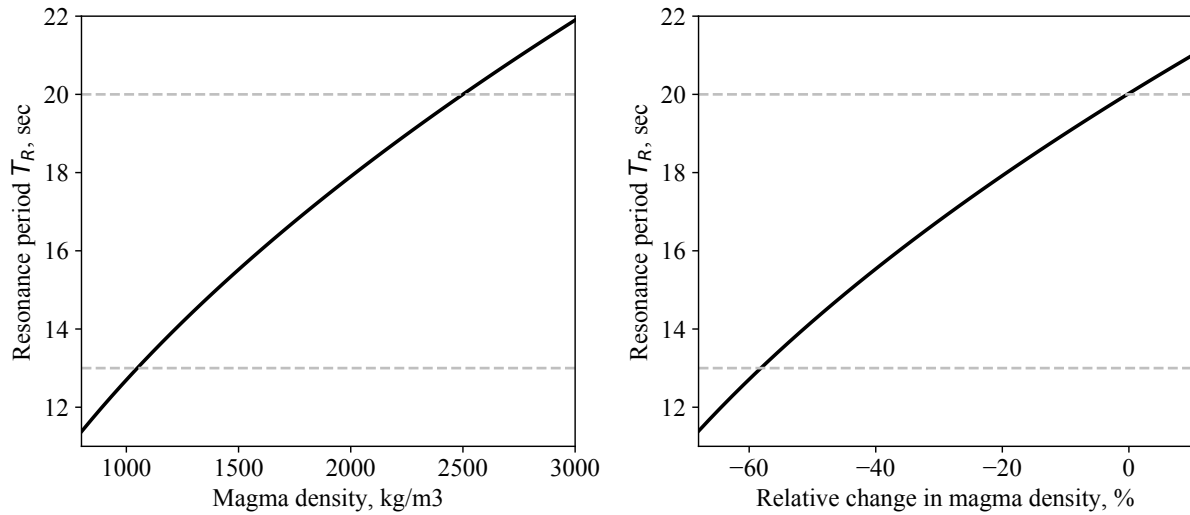


**Fig. S18. Resonance period as a function of the magma density.** We assume a transverse mode  $m=2$ , a dike length  $L=2300$  m, width  $W=1440$  m and thickness  $d=1$  m (see supplementary Text S7). Horizontal dashed grey lines indicate the resonance periods  $T_R = 20$  sec and  $T_R = 13$  sec, observed at the beginning and at the end of the sequence, respectively.

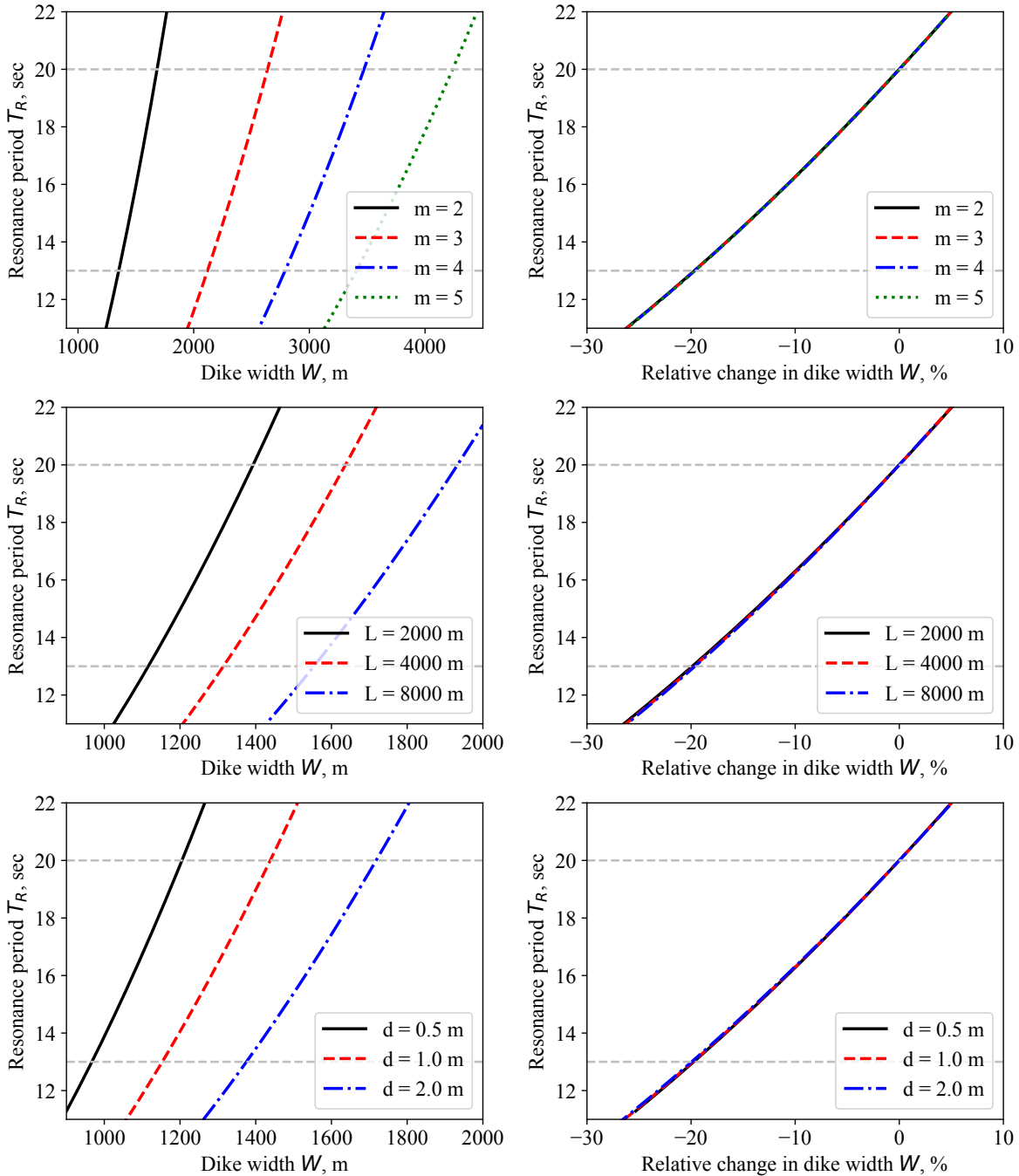


**Fig. S19. Resonance period for different modes and dike geometries.** Left subfigures show the resonance period  $T_R$  as a function of the dike width  $W$ . Right plots show  $T_R$  with respect to the relative change in dike width  $(W-W_{20s})/W_{20s}$  where  $W_{20s}$  is the width corresponding to  $T_R=20$  s for each mode  $m$ , dike length  $L$  and dike thickness  $d$ . Top plots show  $T_R$  predicted for different modes  $m$  assuming  $L=4500$  m and  $d=1$  m. Middle plots show  $T_R$  for different dike lengths  $L$  assuming  $m=2$  and  $d=1$  m. Bottom subfigures show  $T_R$  for different dike thicknesses  $d$  assuming  $m=2$  and  $L=2300$  m. Note that all curves collapse on a single curve when considering the variation of  $T_R$  as a function of the relative change in dike width.

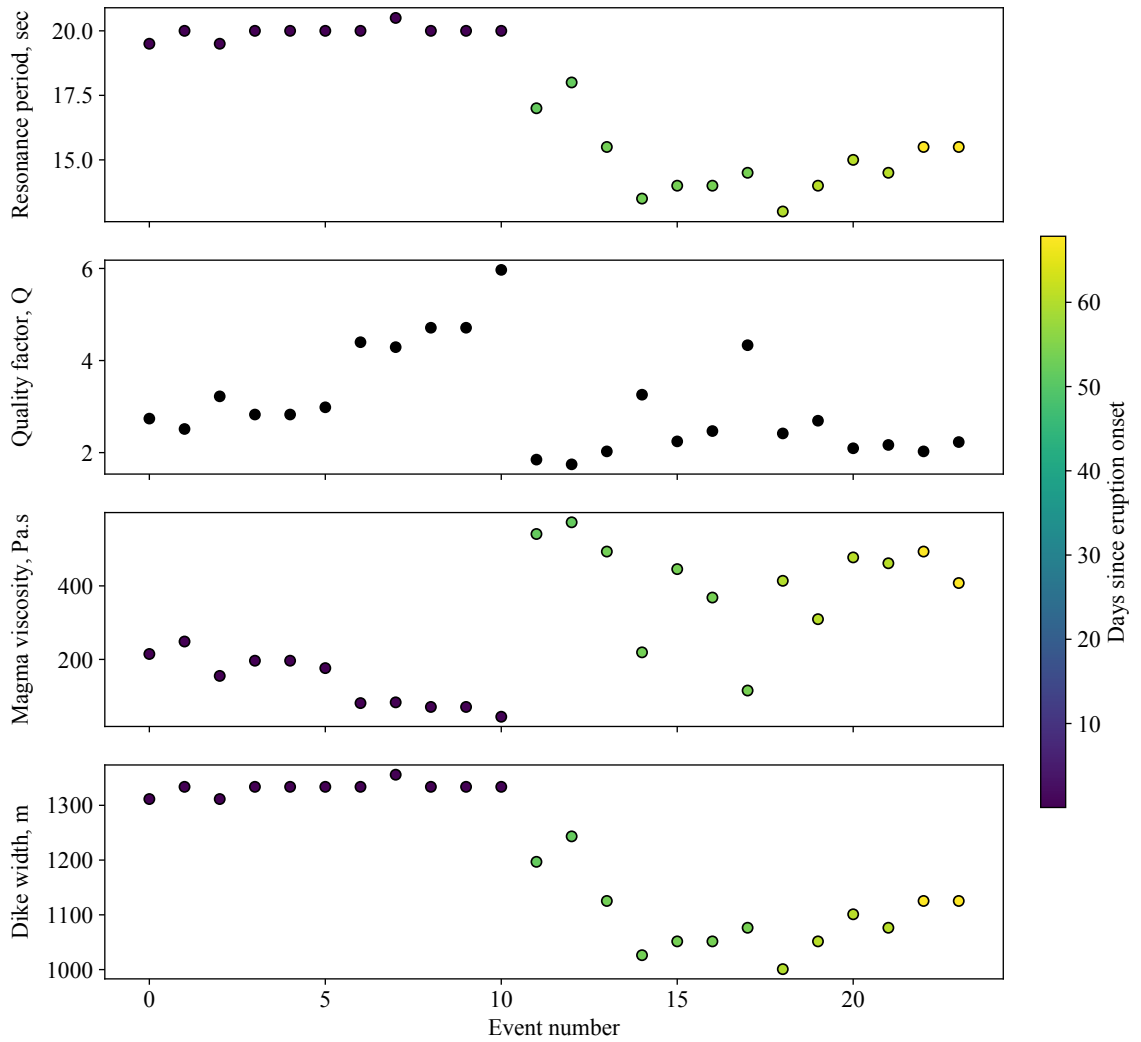


**Fig. S20. Time-evolution of the dike width and magma viscosity.** The two top subfigures shows the time-evolution of resonance period and quality factor estimated from our source inversions. The two bottom subfigures indicate the time-evolution of the magma viscosity and the dike width using the expressions of Lipovsky and Dunham (2015) for the fundamental mode in the boundary layer crack wave limit.

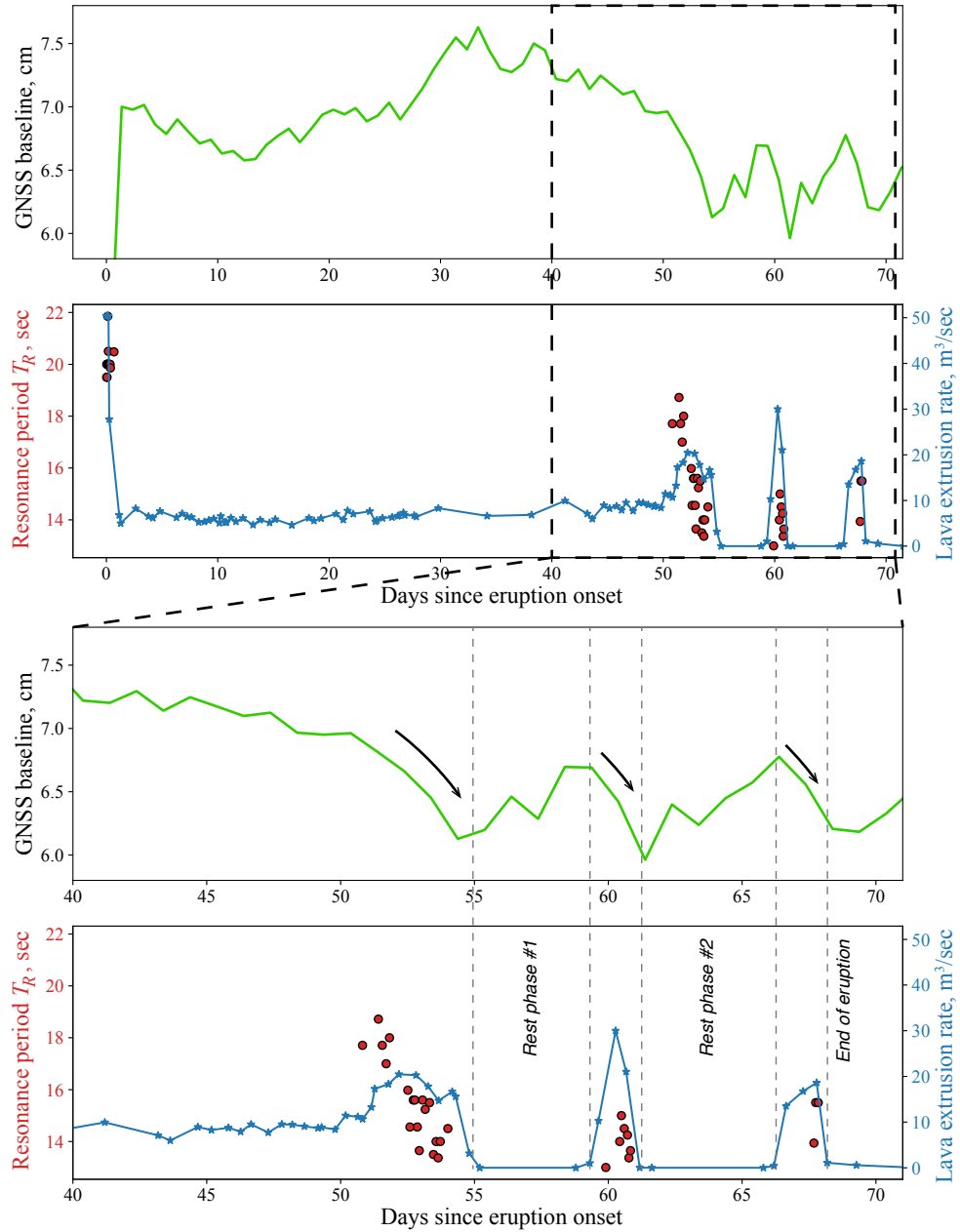


**Fig. S21. Time-evolution of the resonance period (red circles), GNSS baseline (green line) and Time-Average lava Discharge Rate (TADR, blue stars) during the August-October 2015 eruption.** Top two subfigures show the time-evolution over the entire eruption. Bottom subfigures are a zoom over the last month of eruptive activity. Grey dashed vertical lines in the bottom subplots indicate the rest phases and end of the eruption. Black arrows outline deflation episodes concomitant with VLP swarms in October 2015.

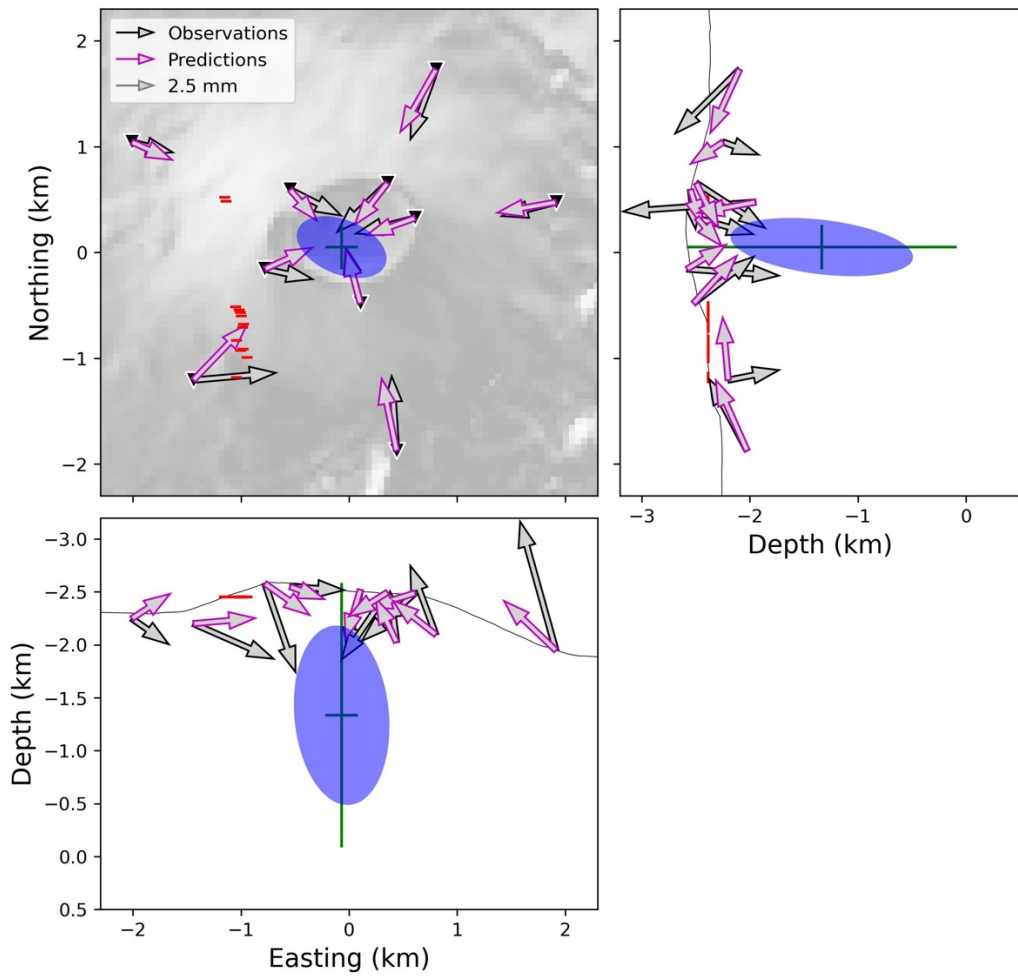


**Fig. S22. Point compound dislocation model of the summit deflation in October 2015.** This solution was obtained by inverting GNSS displacements between October 13 and October 17, 2015 (see Text S2). Observed and Predicted GNSS displacements are shown respectively by black and purple arrows. The best fitting ellipsoid associated with a volume variation  $\Delta V = -0.17 \text{ Mm}^3$  is shown in blue with location errorbars in green.

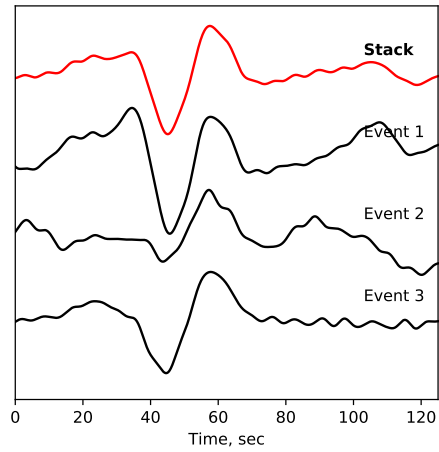


**Fig. S23. VLP detected during the June 2014 eruption.** Data is bandpass filtered between 0.01 and 0.05Hz. The top red trace is the stack of the waveforms shown below.

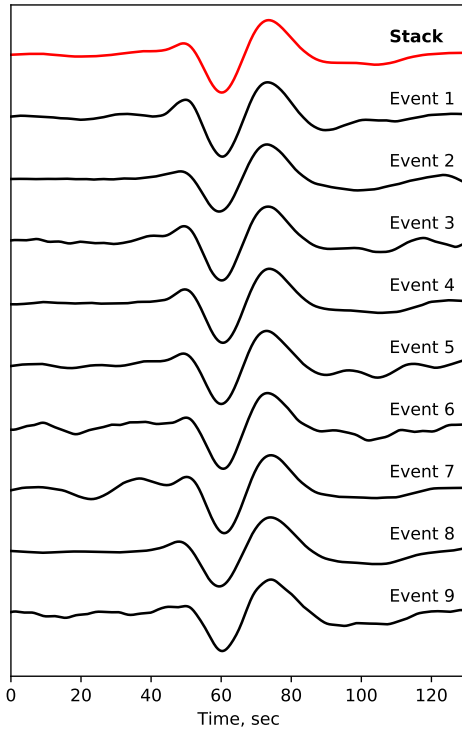


**Fig. S24. VLP detected during the February 2015 eruption.** Data is bandpass filtered between 0.01 and 0.05Hz. The top red trace is the stack of the waveforms shown below.

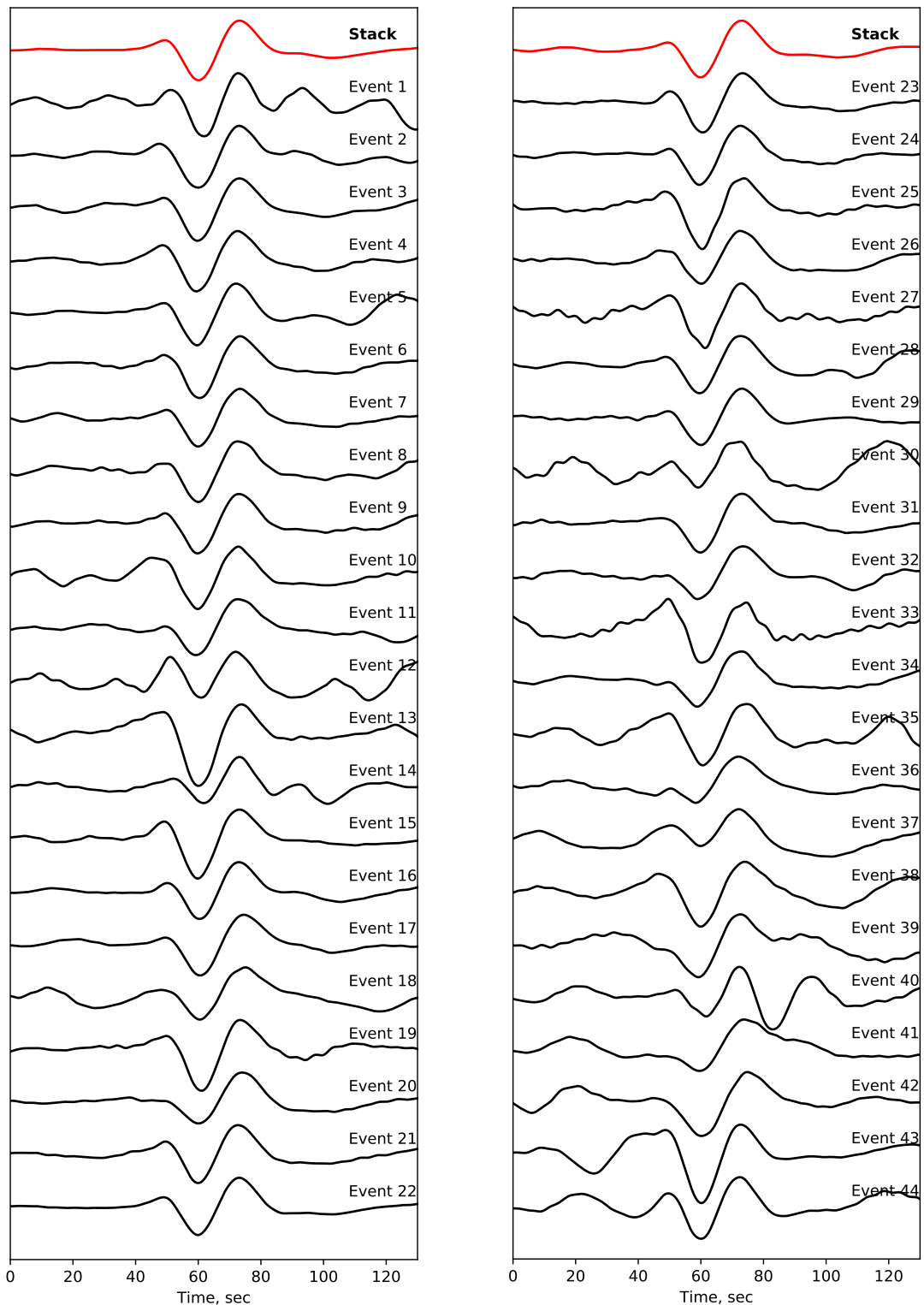


**Fig. S25. VLP detected during the May 2015 eruption.** Data is bandpass filtered between 0.01 and 0.05Hz. The top red trace is the stack of the waveforms shown below.

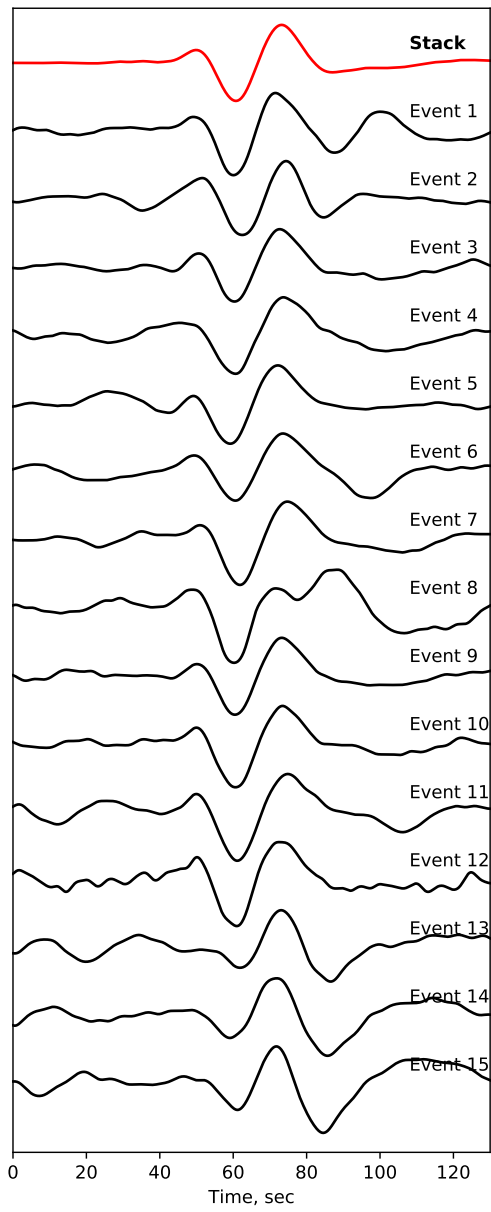


**Fig. S26. VLP detected during the July-August 2015 eruption.** Data is bandpass filtered between 0.01 and 0.05Hz. The top red trace is the stack of the waveforms shown below.

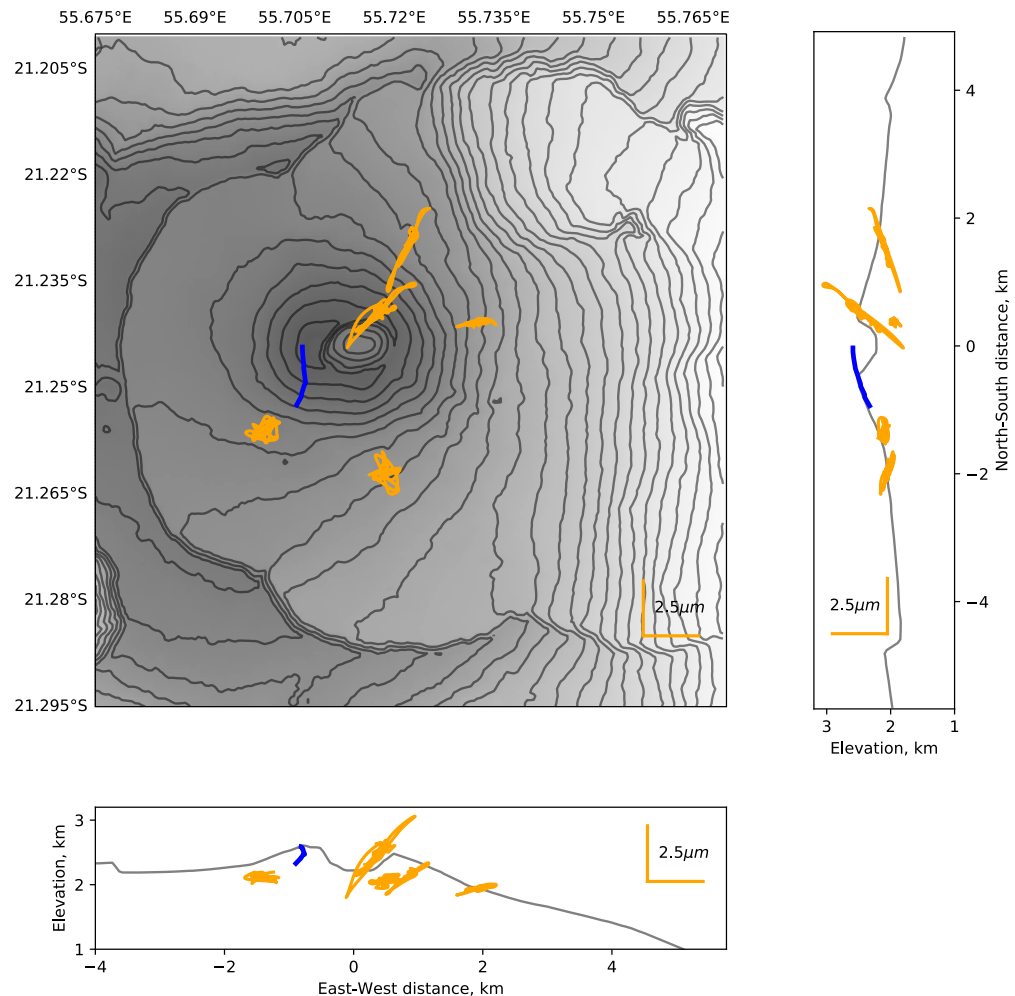


**Fig. S27. Example of particle motions for a VLP event during the February 2015 eruption** (detection time: 2015-02-04T08:22:09 UTC). Particle motion is shown in orange in map view, East-West and North-South cross-sections. Blue lines indicate the location of eruptive fissures for this eruption.

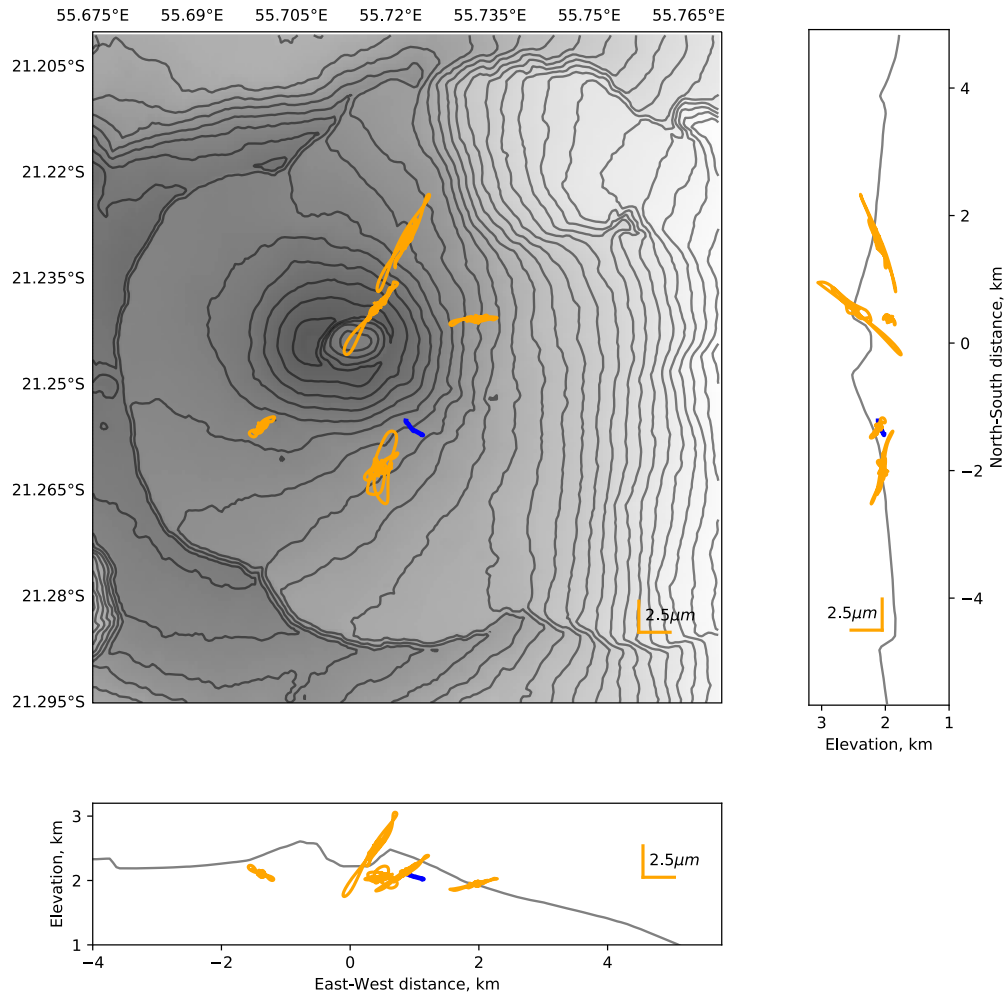


**Fig. S28. Example of particle motions for a VLP event during the May 2015 eruption** (detection time: 2015-05-17T12:51:05 UTC). Particle motion is shown in orange in map view, East-West and North-South cross-sections. Blue lines indicate the location of eruptive fissures for this eruption.

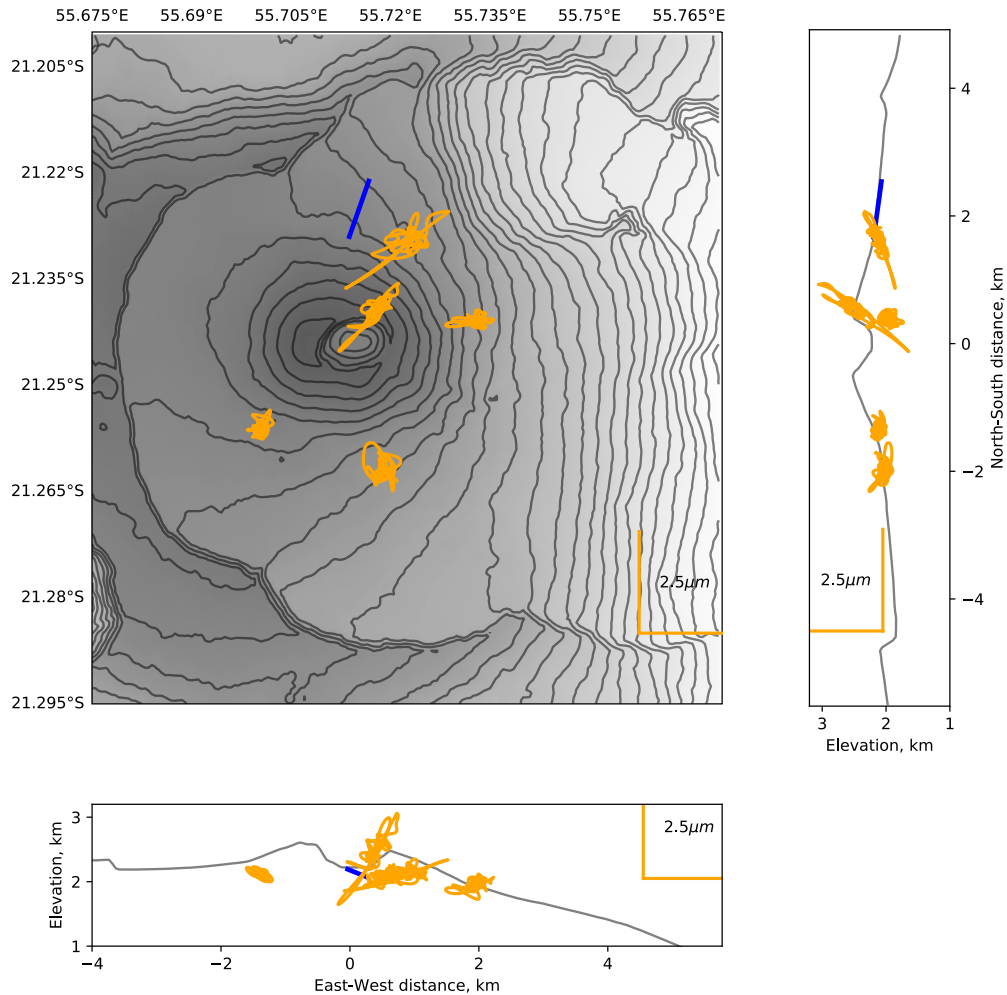


**Fig. S29. Example of particle motions for a VLP event during the July-August 2015 eruption** (detection time: 2015-07-31T08:10:04 UTC). Particle motion is shown in orange in map view, East-West and North-South cross-sections. Blue lines indicate the location of eruptive fissures for this eruption.

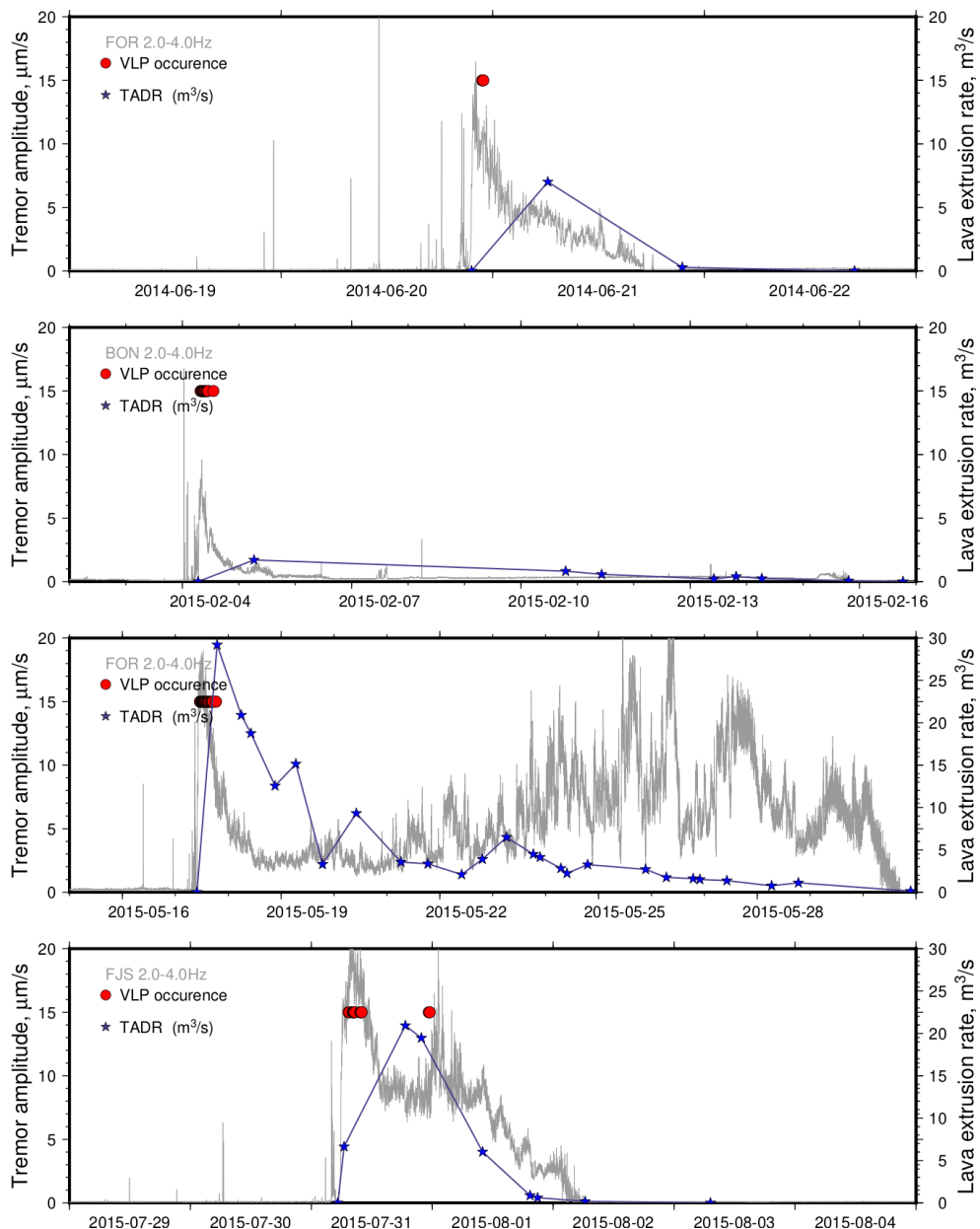


**Fig. S30. VLP events detected during eruptions on June 2014, February 2015, May 2015 and July-August 2015 at Piton de la Fournaise.** Same as Fig. 3: Red dots are VLP detection times, Grey lines indicate the tremor amplitude and blue stars show TADR measurements.